

Parameterizing mesoscale eddy buoyancy transport over sloping topography

Aleksi Nummelin^{1,2,3} and Pål Erik Isachsen^{1,4}

¹University of Oslo

²Finnish Meteorological Institute

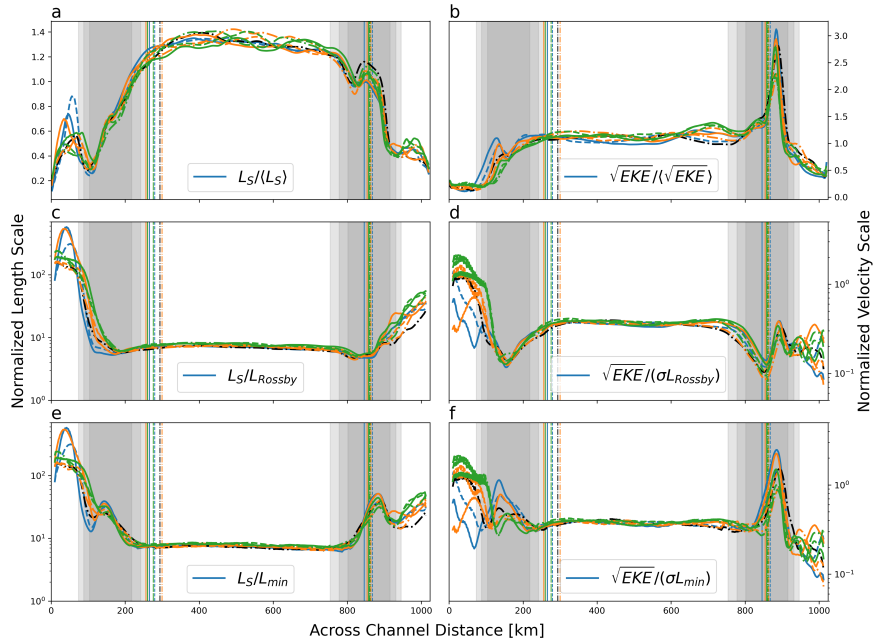
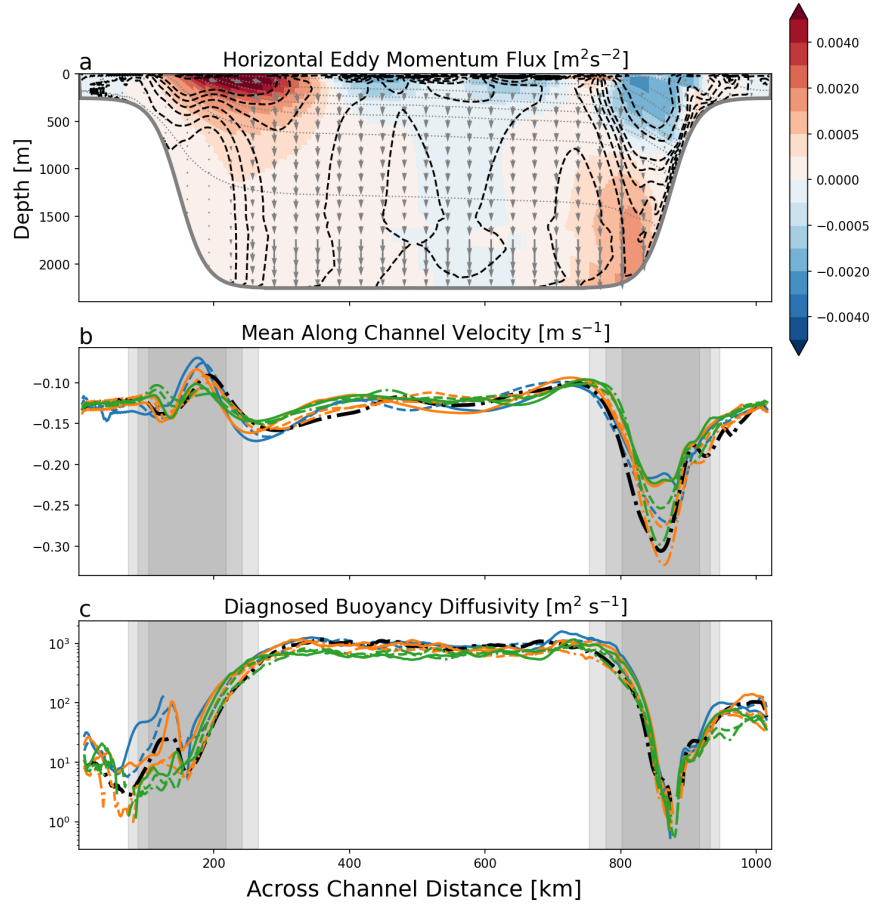
³NORCE Norwegian Research Centre AS

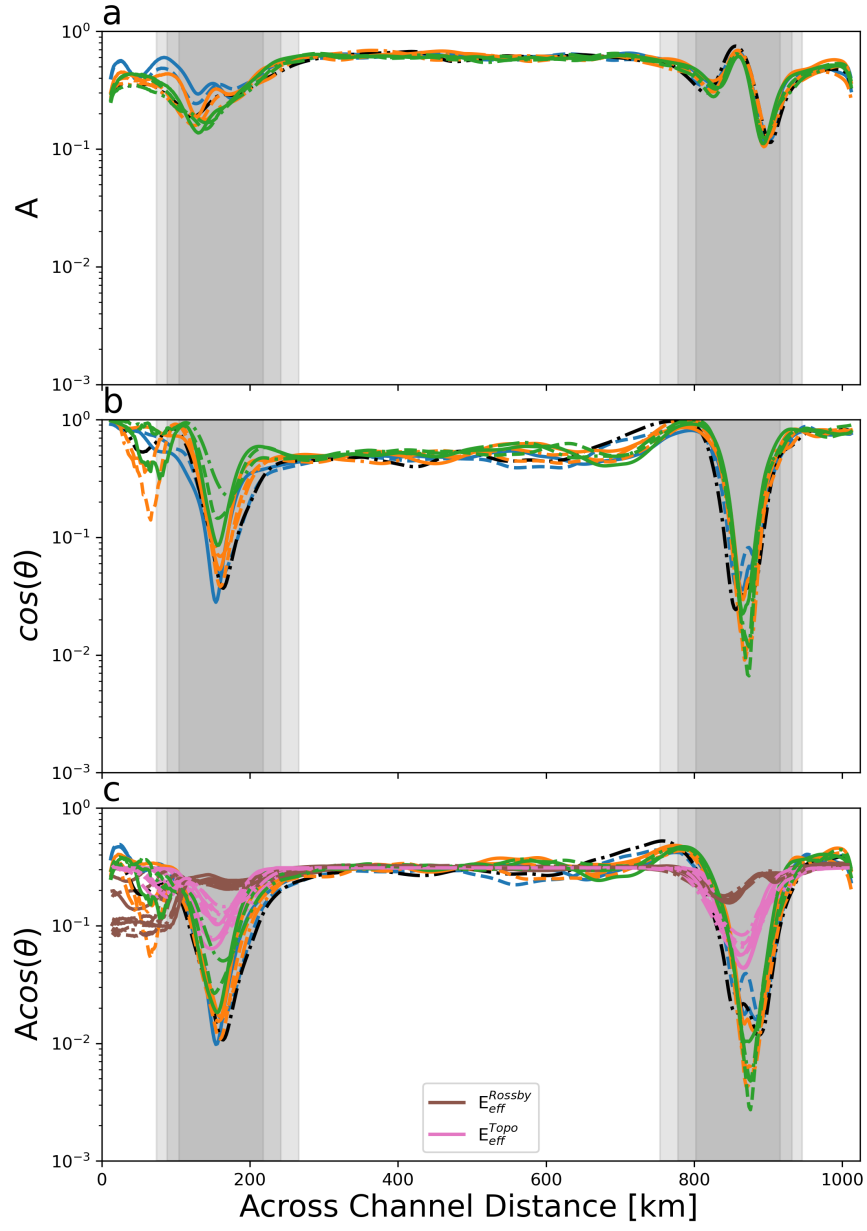
⁴Norwegian Meteorological Institute

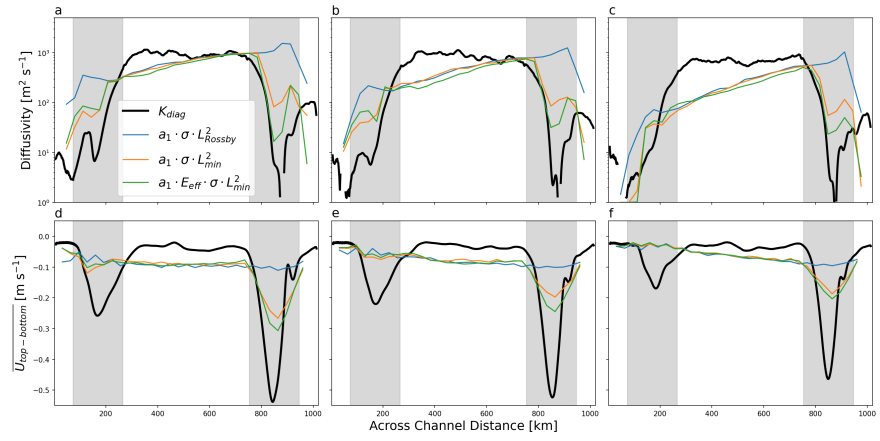
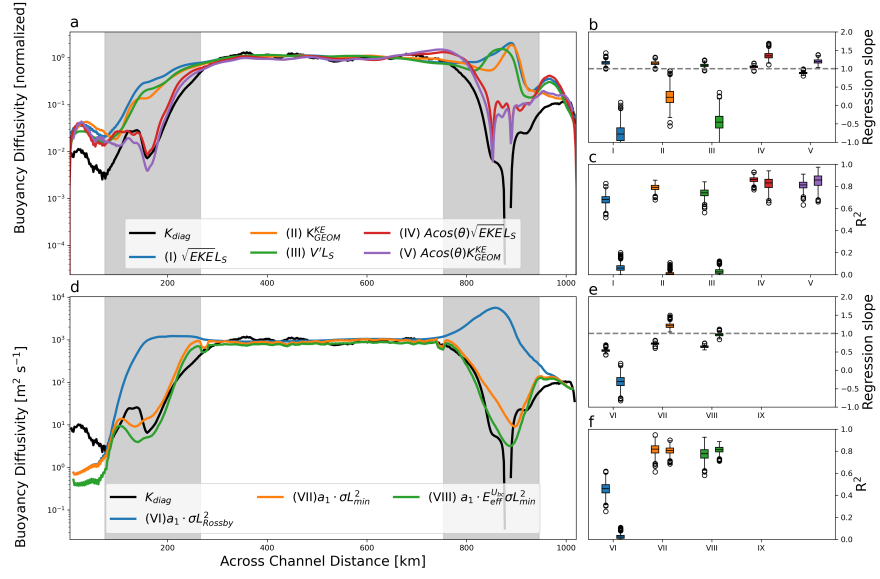
January 16, 2024

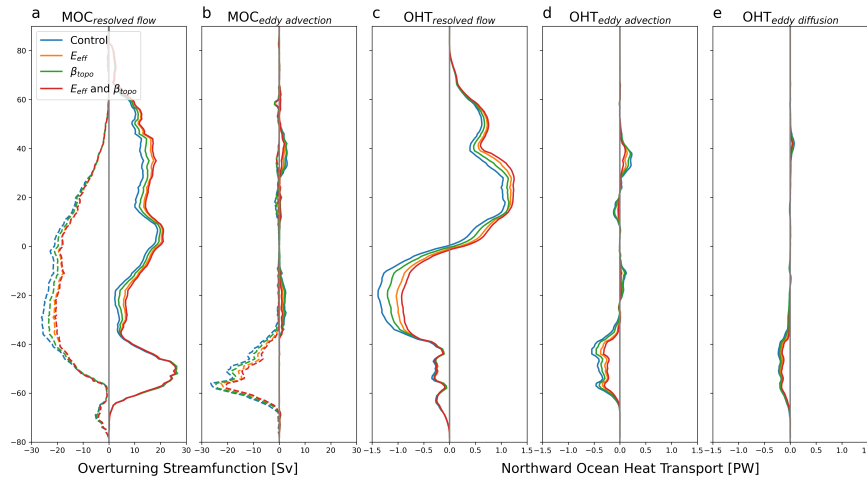
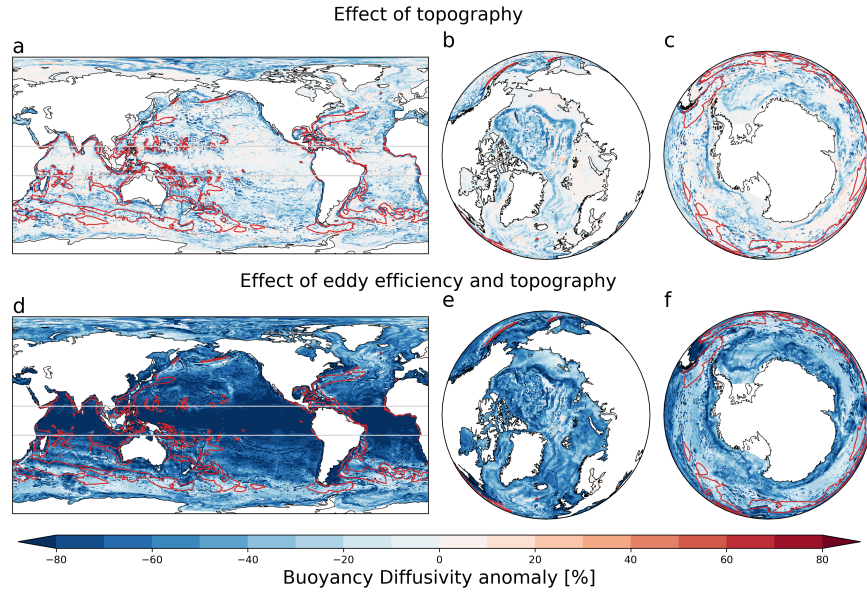
Abstract

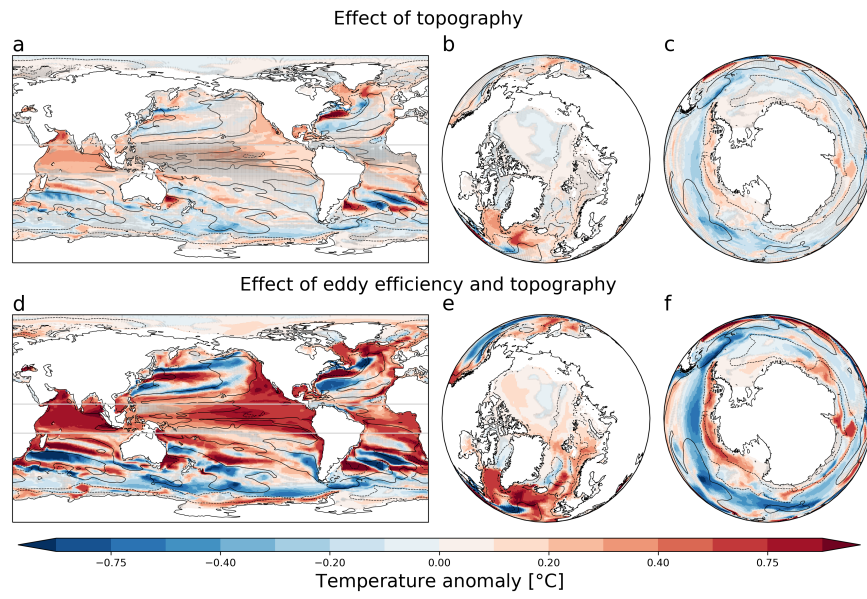
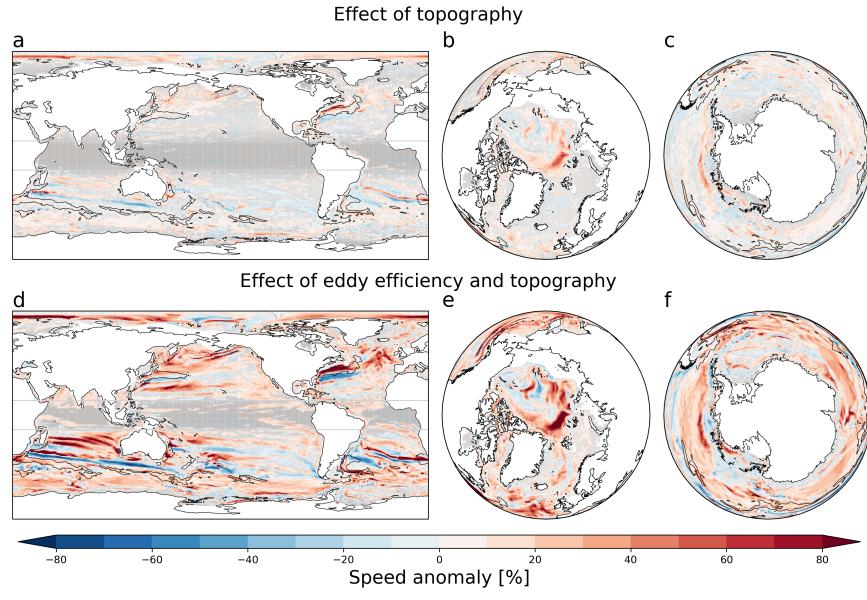
Most of the ocean’s kinetic energy is contained within the mesoscale eddy field. Models that do not resolve these eddies tend to parameterize their impacts such that the parameterized transport of buoyancy and tracers reduces the large-scale available potential energy and spreads tracers. However, the parameterizations used in the ocean components of current generation Earth System Models (ESMs) rely on an assumption of a flat ocean floor even though observations and high-resolution modelling show that eddy transport is sensitive to the potential vorticity gradients associated with a sloping seafloor. We show that buoyancy transport coefficient diagnosed from idealized eddy-resolving simulations is indeed reduced over both prograde and retrograde bottom slopes (topographic wave propagation along or against the mean flow, respectively) and that the reduction can be skilfully captured by a mixing length parameterization by introducing the topographic Rhines scale as a length scale. This modified ‘GM’ parameterization enhances the strength of thermal wind currents over the slopes in coarse-resolution, non-eddy, simulations. We find that in realistic global coarse-resolution simulations the impact of topography is most pronounced at high latitudes, enhancing the mean flow strength and reducing temperature and salinity biases. Reducing the buoyancy transport coefficient further with a mean-flow dependent eddy efficiency factor, has notable effects also at lower latitudes and leads to reduction of global mean biases.

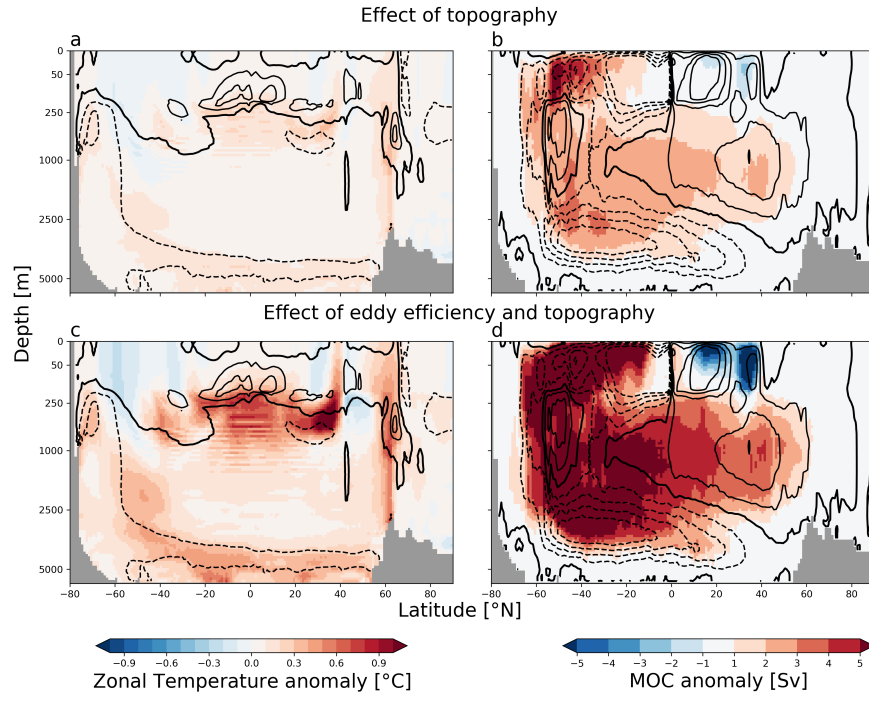












Parameterizing mesoscale eddy buoyancy transport over sloping topography

Aleksi Nummelin^{1,2,3}, Pål Erik Isachsen^{1,4}

¹University of Oslo, Department of Geosciences, Oslo, Norway

²NORCE Norwegian Research Centre AS and Bjerknes Centre for Climate Research, Bergen, Norway

³Finnish Meteorological Institute, Helsinki, Finland

⁴Norwegian Meteorological Institute, Oslo, Norway

Key Points:

- Eddy buoyancy diffusivity reduction over bottom slopes can be parameterized using the Eady growth rate and topographic Rhines scale.
- Realistic reduction in buoyancy diffusivity in a coarse-resolution model strengthens baroclinic boundary currents.
- A topographically-aware eddy efficiency factor improves the parameterization and further reduces biases in global simulations.

Corresponding author: Aleksi Nummelin, aleksi.nummelin@fmi.fi

Abstract

Most of the ocean’s kinetic energy is contained within the mesoscale eddy field. Models that do not resolve these eddies tend to parameterize their impacts such that the parameterized transport of buoyancy and tracers reduces the large-scale available potential energy and spreads tracers. However, the parameterizations used in the ocean components of current generation Earth System Models (ESMs) rely on an assumption of a flat ocean floor even though observations and high-resolution modelling show that eddy transport is sensitive to the potential vorticity gradients associated with a sloping seafloor. We show that buoyancy transport coefficient diagnosed from idealized eddy-resolving simulations is indeed reduced over both prograde and retrograde bottom slopes (topographic wave propagation along or against the mean flow, respectively) and that the reduction can be skilfully captured by a mixing length parameterization by introducing the topographic Rhines scale as a length scale. This modified ‘GM’ parameterization enhances the strength of thermal wind currents over the slopes in coarse-resolution, non-eddying, simulations. We find that in realistic global coarse-resolution simulations the impact of topography is most pronounced at high latitudes, enhancing the mean flow strength and reducing temperature and salinity biases. Reducing the buoyancy transport coefficient further with a mean-flow dependent eddy efficiency factor, has notable effects also at lower latitudes and leads to reduction of global mean biases.

Plain Language Summary

Due to their high computational costs, global climate models are usually run at coarse spatial resolution, which does not allow them to resolve the ocean weather—mesoscale eddies—which are an important part of the ocean energy cycle and contribute to mixing of tracers such as heat and carbon. Eddies are instead parameterized in an idealized manner which relates the eddy-driven transport to the strength of the vertical and horizontal density gradients in the ocean. Such parameterizations do not take into account impacts of large-scale bottom bathymetry which have been shown to weaken the eddy driven transport. Here we use high-resolution eddy-resolving simulations to improve existing parameterizations so that they become sensitive to the bottom slope. We show that such a parameterization qualitatively captures the transport reduction seen in idealized high-resolution simulations and can also reduce errors in realistic global simulations.

1 Introduction

At present, the ocean components of most global climate models are used at resolutions that require parameterizing transport by the oceanic mesoscale (Fox-Kemper et al., 2019). Although coupled simulations with eddy ocean fields are slowly emerging (Chang et al., 2020), mesoscale eddy parameterizations are still likely part of ocean models for another decade. The wave-turbulence duality of mesoscale eddy dynamics can cause very rich transport behavior, involving intermittency, non-local transport by coherent vortices and even up-gradient fluxes that energize the mean flow (e.g. Chen et al., 2014; Yankovsky et al., 2022; Liu et al., 2023). Nonetheless, most present-day parameterizations do not include such effects, but have their origins in the works of Gent and McWilliams (1990); Gent et al. (1995) and Redi (1982), tackling eddy-induced advection and tracer mixing, respectively. The ‘GM’ advection is specified by an overturning streamfunction which itself is cast in terms of a horizontally down-gradient and vertically up-gradient buoyancy transport—resulting in a reduction of available potential energy. ‘Redi’ diffusion, by contrast, mixes both active and passive tracers down-gradient along isopycnals (Gent, 2011).

Much of the current research focuses on how to prescribe flow-dependent eddy transport coefficients, or eddy ‘diffusivities’, that set the strength of the GM advection and

65 Redi mixing. These are distinct processes, and the vertical structure of eddy buoyancy
66 transport certainly appears to be different from that of isopycnal Redi diffusion, includ-
67 ing the diffusion of potential vorticity (PV) (see e.g. K. S. Smith & Marshall, 2009; Aber-
68 nathey et al., 2013; Bachman et al., 2020). Less is known about how GM and Redi dif-
69 fusivities relate laterally, but since both are sensitive to e.g. eddy energy levels, we ex-
70 pect them be spatially correlated. In practice, the diffusivities, whether applied to the
71 GM or Redi scheme, are most often parameterized following mixing length theory. This
72 means that they are constructed from the product of some eddy velocity scale and a mix-
73 ing length scale. Some work has gone into estimating the eddy velocity scale by imple-
74 menting a prognostic equation for eddy energy (Eden & Greatbatch, 2008; Marshall et
75 al., 2012; Mak et al., 2018; Bachman, 2019; Jansen et al., 2019), but this is still very much
76 an active and incomplete field of research. So, in the latest iteration of the Climate Model
77 Inter Comparison Project (CMIP; <https://explore.es-doc.org/cmip6/models/>), the
78 GFDL-CM4.0 model (Adcroft et al., 2019) was, to our knowledge, the only one that used
79 a prognostic eddy energy approach to estimate the eddy velocity scale.

80 The study by Visbeck et al. (1997) therefore continues to influence the practical
81 use of the mixing length approach. Drawing on earlier works by Green (1970) and Stone
82 (1972), they proposed that the velocity scale for the GM diffusivity be based on the prod-
83 uct of the growth rate of baroclinic instability in the linearized Eady model (Eady, 1949)
84 and some length scale. Assuming that the mixing length is also set by the same scale,
85 the diffusivity will then scale as the Eady growth rate and the square of the length scale.
86 Visbeck et al. (1997) associated the mixing length with the ‘width of the baroclinic zone’
87 which they defined as “the width of the region where the local growth rate exceeds 10%
88 of the maximum growth rate of the field”. The concept, however, is hard to define in any
89 but the most idealized model geometries, and length scales therefore need to be formed
90 from more rigorous dynamical arguments.

91 As proposed by Stone (1972), one obvious candidate for length scale is the inter-
92 nal deformation radius, the approximate scale of the fastest unstable growth in the Eady
93 model. Solid observational evidence for the relevance of this length scale has been pre-
94 sented by Stammer (1997) and Eden (2007). However, other relevant scales arise if dy-
95 namics beyond the Eady framework are accounted for, most notably bottom friction and
96 potential vorticity (PV) gradients. Jansen et al. (2015), for example, examined the role
97 of bottom friction and the planetary vorticity gradient in a two-layer flat-bottom chan-
98 nel model. They found that bottom friction primarily influences the vertical distribu-
99 tion of eddy energy and that the mixing length in most of their simulations is set by the
100 Rhines scale, i.e. the transition scale between nonlinear and linear PV dynamics on the
101 flat-bottom planetary beta plane (Rhines, 1977). More generally, Jansen et al. (2015)
102 found that in order to cover various dynamical regimes, the smaller of several candidate
103 length scales should be chosen, and that inclusion of the Rhines scale amongst these scales
104 is important. In fact, the observational studies of both Stammer (1997) and Eden (2007)
105 specifically pointed to a minimum of the internal deformation radius and the Rhines scale
106 as a best fit for eddy length scales over much of the world ocean.

107 These principles remain the standard in state-of-the-art models, although devel-
108 opment has occurred in later years. As mentioned above, there has been extensive fo-
109 cus on developing prognostic equations for eddy energy. Considerable efforts have also
110 gone into studying effects of horizontal eddy anisotropy (R. D. Smith & Gent, 2004) and
111 the suppression of mixing across strong mean flows (Ferrari & Nikurashin, 2010; Klocker
112 et al., 2012, and references therein). It’s worth noting, however, that most of the devel-
113 opment up until recently has been guided by observed dynamics in low and mid latitudes.
114 Current parameterizations thus lack any treatment of two aspects that are potentially
115 of huge importance in high latitude oceans, namely the presence of sea ice and the po-
116 tential vorticity gradients imposed by sloping bottom topography. A sea ice cover can
117 effectively have the same influence as bottom friction on growth of baroclinic instabil-

ity as well as on dissipation of existing mesoscale and sub-mesoscale eddies (Meneghello et al., 2021). This topic, however, will be left out from the present study. We will instead focus on the dynamical impacts of bottom slopes, i.e. continental slopes and mid-ocean ridge systems, whose imprints can be easily seen in observations of both mean currents and mesoscale energy fields, especially at high northern latitudes (Nøst & Isachsen, 2003; Koszalka et al., 2011; Trodahl & Isachsen, 2018). Imprints of topographic PV gradients can also be seen at lower latitudes, e.g. in drifter and float paths (LaCasce, 2000; Frantoni, 2001).

Sloping bottom topography can suppress growth rate and reduce length scales of baroclinic instability (e.g. Blumsack & Gierasch, 1972; Mechoso, 1980; Isachsen, 2011; Brink, 2012) as well as impact finite-amplitude eddy fields (e.g. Bretherton & Haidvogel, 1976; Vallis & Maltrud, 1993; Lacasce & Brink, 2000; K. Stewart et al., 2015; Wang & Stewart, 2018). To this end, new topography-aware parameterizations have started to emerge, both for eddy-induced advection and isopycnal mixing. In particular, Wang and Stewart (2020) and Wei et al. (2022) tested different scaling relations for the GM diffusivity in high-resolution model simulations of flows over idealized continental slopes in re-entrant channels. The two works examined eddy characteristics and fluxes across retrograde and prograde mean currents, respectively, meaning currents that are in the opposite and same direction as topographic waves. Both studies diagnosed the eddy energy from the high-resolution fields and used this to examine traditional mixing length formulations, trying out various choices for mixing length. In addition, they tested the ‘GEOMETRIC’ formulation of Marshall et al. (2012) in which diffusivities are instead constructed from eddy energy and an eddy decorrelation time scale which is set equal to the inverse of the Eady growth rate. In general, the two formulations performed similarly, suggesting that a good knowledge of the eddy energy field is key. However, importantly, both studies also found that empirical prefactors that depend on the topographic slope are needed to reproduce very weak eddy buoyancy fluxes across sloping bottom topography.

Wei and Wang (2021) carried on from Wang and Stewart (2020), but focused on the along-isopycnal tracer (Redi) diffusivity in the same channel model—in retrograde flows only. The authors constructed a parameterized Redi diffusivity from (the square root of) the diagnosed eddy kinetic energy and the internal deformation radius, again finding that the actual diffusivity over the slope was suppressed below the original scale estimate. However, instead of testing a set of empirical slope-dependent prefactors, as done by Wang and Stewart (2020) and Wei et al. (2022), this study picked up from Ferrari and Nikurashin (2010) and demonstrated that mean-flow suppression could explain the observed reduction in cross-slope fluxes near the surface, whereas eddy velocity anisotropy contributed to the reduction close to the bottom.

In other words, both sets of studies (see also Brink, 2012, 2016; Hetland, 2017) concluded that eddy diffusivities over sloping bottoms are poorly reproduced by traditional open-ocean scaling choices for eddy velocity and eddy length (or decorrelation time), and that additional dynamical impacts of the bottom topography must be brought in. Topographically-induced velocity anisotropy is one obvious factor which could impact both the effective eddy velocity (its orientation relative to the tracer gradient) and effective mixing length or time scale. In addition, mean-flow suppression, caused by eddies propagating relative to the mean flow, may also be reflected in a reduced effective mixing length, as suggested by Ferrari and Nikurashin (2010, their equation 13). But such interpretations have so far only been applied to Redi diffusion—now also over continental slopes (Wei & Wang, 2021). Whether similar dynamics lie behind the various empirically-fitted suppression factors in the studies of buoyancy diffusion over continental slopes is yet an open question.

The present study will primarily focus on eddy buoyancy transport and thus on GM diffusivities. It is inspired by and builds directly on the results obtained by Wang

171 and Stewart (2020) and Wei et al. (2022), and, as they did, we thus limit the scope to
 172 depth-averaged diffusivities. However, as noted, the above works examined prograde and
 173 retrograde flows separately and also constructed diffusivities from eddy energy levels di-
 174 agnosed from very idealized but high-resolution fields. So here we aim to i) study fluxes
 175 and diffusivities over both types of flow situations under one and the same framework,
 176 ii) examine how far one can get with parameterizations that do not rely on diagnosing
 177 the actual eddy energy field and, finally, iii) expand by assessing impacts both in an ide-
 178 alized setting and in a realistic global ocean simulation.

179 In the process, we revisit the question of what is the relevant eddy mixing length
 180 over continental slopes. The starting point will be the internal deformation radius since
 181 this remains a relevant parameter in the Eady problem. In addition, we also consider
 182 the topographic Rhines scale, i.e. the scale that marks the transition between a linear
 183 topographic Rossby wave (rather than planetary Rossby wave) regime and turbulent PV
 184 dynamics. The above-mentioned idealized channel studies give conflicting evidence about
 185 the relevance of this scale. We are nevertheless inspired by the findings of Stammer (1997),
 186 Eden (2007) and Jansen et al. (2015) and bring up this approach here again. To home
 187 in on what actually goes on over the slopes, we will also diagnose the eddy velocity anisotropy
 188 and, in addition, the phase relationship between velocity and tracer perturbations. This
 189 second diagnostic gives additional information about dynamics not reflected in mere scale
 190 estimates, at least estimates of eddy velocity. Essentially, no matter how strong the Root
 191 Mean Square (RMS) eddy velocity is, if velocity perturbations are in quadrature with
 192 buoyancy perturbations a zero transport results. The analysis done here will indeed show
 193 that most of the topographic suppression is reflected in a degraded phase relationship
 194 and that velocity anisotropy takes on a secondary role.

195 The paper is structured as follows: In section 2 we introduce the modelling tools
 196 and various diagnostics and parameterizations used. In section 3 we begin by diagnos-
 197 ing eddy fields from high-resolution channel simulations that contain both prograde and
 198 retrograde flows at the same time. We then see how far mixing-length and GEOMET-
 199 RIC parameterizations can take us in reproducing the diagnosed depth-averaged GM diffusivity—
 200 with and without accounting for effect of anisotropy and phase relations between eddy
 201 velocity and tracer perturbations. At the end of this section we examine the impact of
 202 a topographically-aware parameterization in a coarse-resolution version of the channel
 203 model. In section 4 we finally employ the new parameterization in realistic global ocean
 204 simulation. We then take a critical look into some of our parameterization choices and
 205 their interpretation in section 5 before summarizing our findings in section 6.

206 **2 Methods**

207 **2.1 Model setup**

208 We use the Bergen Layered Ocean Model (BLOM), the ocean component of the
 209 Norwegian Earth System Model (NorESM; Seland et al., 2020), in an idealized channel
 210 configuration as well as in a realistic global setup (both configurations are published in
 211 Nummelin, 2023b). BLOM uses 51 isopycnal levels (potential density referenced to 2000 dbar)
 212 with a 2-level bulk mixed layer at the surface. In order to diagnose the various quanti-
 213 ties used in the study, we interpolate the outputs locally (in time and space) to height
 214 coordinates, except for quantities that are specifically calculated from isopycnal output
 215 (see below), in which case we interpolate the outputs to a new density grid so that the
 216 bulk mixed layer is properly accounted for.

217 The channel setup is re-entrant in the zonal (x) direction. The domain is 416 km
 218 long (zonally) and 1024 km (y_{max}) wide (meridionally). At both sides of the channel there
 219 are continental slopes of given width (W) centered at 150 km (Y_C) from the domain edges,
 220 stretching 2000 m (D_S) in the vertical from the shelf break at 250 m depth (D_B) to the

221 bottom of the slope at 2250 m depth. These parameters then define the bathymetry (H)
 222 across the channel (along the y -coordinate):

$$223 \quad H(y) = \begin{cases} D_B + 0.5 \cdot D_S \left\{ 1 + \tanh \left[\frac{\pi(y - Y_C)}{W} \right] \right\}, & y < (Y_C + W) \\ D_B + 0.5 \cdot D_S \left\{ 1 + \tanh \left[\frac{\pi(y_{max} - y - Y_C)}{W} \right] \right\}, & y_{max} - y < (Y_C + W) \\ D_B + D_S, & \text{otherwise i.e. in the central basin.} \end{cases}$$

224 In addition, to trigger instabilities we add 2D random noise with standard deviation of
 225 10 m to the bottom topography.

226 The model is initialized from rest with constant salinity and a horizontally homo-
 227 geneous temperature profile. The temperature, which here determines density alone, has
 228 a maximum at the surface and decays exponentially towards the bottom. We place the
 229 channel in the northern hemisphere, using a constant Coriolis parameter, and then force
 230 the flow with a constant westward wind stress. The surface mixed layer is kept shallow
 231 by parameterization of submesoscale mixed layer eddies (Fox-Kemper et al., 2008) that
 232 counter the vertical mixing induced by the constant wind forcing. See Table 1 for fur-
 233 ther parameter settings.

234 We first run the channel model at 2 km horizontal resolution, which is eddy-resolving
 235 over the deep central basin and over the slopes (see Table 2 for deformation radius) but
 236 only eddy-permitting over the shallow shelves. To investigate the effects of the two bot-
 237 tom slopes on eddy transport and, specifically, on eddy diffusivity, we vary the initial strat-
 238 ification and the width of the continental slope, i.e the slope angle. The various exper-
 239 iments are laid out in Table 2. All simulations are spun-up for 10 years to a semi-equilibrium
 240 in which domain averaged eddy kinetic energy is close to constant, and the model fields
 241 are then diagnosed over an additional 5-year period (so between years 11–15). We then
 242 test and compare various forms of parameterized eddy buoyancy fluxes at non-eddying
 243 32 km resolution in the same idealized channel. These are also run for 15 years, with the
 244 last 5 years being diagnosed. With the focus on the 5-year means, we are assuming a slowly-
 245 varying eddy field and attempting to parameterize its time-mean impact. However, we
 246 note that geostrophic turbulence is known to be intermittent with implications for vari-
 247 ability in eddy transport and mixing (Busecke & Abernathey, 2019; Huneke et al., 2019;
 248 G. Zhang et al., 2023; Ong et al., 2023). Also our simulations suggest that over the north-
 249 ern prograde slope the jet there undergoes periods of alternating strong and weak eddy
 250 activity on a timescale of several months (not shown). How the time-mean view of the
 251 eddy transport presented here incorporates such variability is left for future studies.

252 Finally, the impact of the most skillful parameterization is assessed in realistic global
 253 simulations. These are nominal 1° resolution global forced ocean-ice experiments which
 254 follow the Ocean Model Intercomparison Project, OMIP-II protocol (Tsujino et al., 2020).
 255 In these simulations, the mean grid size north of 62°N and south of 64.5°S is approx-
 256 imately 32 km, similar to the coarse resolution channel. We compare simulation with an
 257 existing eddy parameterization, which does not include any effects of bottom topogra-
 258 phy, to simulations with parameterizations that feel the bottom topography through the
 259 topographic beta parameter (Figure S1, panel a-c; see section 2.2 for further definitions).
 260 Each simulation is 110 year long (2 cycles of 55 long repeat cycle), and we diagnose the
 261 results using the last 30 years. At this point there is still a long-term drift in the model
 262 (as seen in all models following the OMIP-II protocol; Tsujino et al., 2020), but the gen-
 263 eral circulation has stabilized.

264 2.2 Diagnostics and Parameterizations

265 The key parameter of interest is the buoyancy diffusivity, and in this study, we fo-
 266 cus exclusively on the depth-averaged diffusivity. We leave the development of depth-
 267 varying parameterizations for future studies. A fruitful way forward for this may be to

268 develop a flow-dependent structure function that distributes the depth-averaged diffu-
 269 sivity vertically (see e.g. Bachman et al., 2020; Wei & Wang, 2021).

270 In the idealized zonal channel simulations, where buoyancy is given by tempera-
 271 ture, the cross-channel (i.e. meridional) buoyancy diffusivity is diagnosed from

$$272 \quad K_{diag} = -\frac{1}{H} \int_H^0 \frac{\langle v'T' \rangle}{\partial \langle T \rangle / \partial y} dz, \quad (1)$$

273 where H is bottom depth, v is meridional velocity, and T is meridional temperature. An-
 274 gle brackets indicate a zonal (along-channel) mean and primes indicate deviations from
 275 such mean. So v' and T' are the across-channel velocity and temperature perturbations
 276 from the zonal mean. In (1), the flux gradient relation is evaluated at each level, before
 277 depth averaging. For analysis of the channel simulations, we also average K_{diag} over time.

278 In what follows, we make frequent use of depth-averaged variables, which we note
 279 with $\langle \bar{\cdot} \rangle$. Thus, our eddy kinetic energy density is defined in terms of depth-averaged ve-
 280 locities as

$$281 \quad EKE = \frac{\langle \bar{u}'^2 \rangle + \langle \bar{v}'^2 \rangle}{2}, \quad (2)$$

282 and an velocity anisotropy factor is defined as

$$283 \quad A = \frac{\langle \bar{v}'^2 \rangle}{\langle \bar{u}'^2 \rangle + \langle \bar{v}'^2 \rangle}, \quad (3)$$

284 so that

$$285 \quad \langle \bar{v}'^2 \rangle = 2A \cdot EKE. \quad (4)$$

286 Parameterizing the diffusivity starts with a scale estimate. Two approaches are cur-
 287 rently in use, the traditional mixing length and the GEOMETRIC approach. In the first
 288 approach, we write

$$289 \quad K_{ML} \propto VL, \quad (5)$$

290 where V is a representative eddy velocity scale and L is a representative mixing length.
 291 If complete information exists about the high-resolution eddy fields, it is natural to set
 292 $V = \sqrt{EKE}$ or, more correctly for the cross-channel diffusion we study here, $V = \sqrt{\langle \bar{v}'^2 \rangle}$.
 293 The mixing length may intuitively be thought of as the size of eddies themselves. We
 294 examine this possibility below, estimating L from the shape of velocity spectra. Several
 295 possibilities exist for this (see e.g. Eden, 2007), but here we chose

$$296 \quad L_S = \frac{\int |\hat{v}(k)|^2 k^{-1} dk}{\int |\hat{v}(k)|^2 dk}, \quad (6)$$

297 where $\hat{v}(k)$ is the Fourier component of the depth-averaged cross-channel velocity at wavenum-
 298 ber k . The expression can be thought of as a kinetic energy-weighted mean wavelength
 299 under the spectrum.

300 In the second approach, the energy-based diffusivity estimate of the GEOMETRIC
 301 framework (Marshall et al., 2012; Mak et al., 2018) is constructed as

$$302 \quad K_{GEOM} \propto \sigma_E^{-1} E, \quad (7)$$

303 where σ_E is the Eady growth rate and E is the total eddy energy. The Eady growth rate
 304 is

$$305 \quad \sigma_E = 0.3 \frac{f}{\overline{Ri}^{-1/2}} \quad (8)$$

306 where f is the Coriolis parameter and Ri is the geostrophic Richardson number:

$$307 \quad Ri = \frac{N^2}{|\partial U_g / \partial z|^2}. \quad (9)$$

308 Here

$$309 \quad N^2 = -\frac{g}{\rho_0} \frac{\partial \rho}{\partial z} \quad (10)$$

$$= \partial b / \partial z$$

310 is the squared buoyancy frequency (g is gravitational acceleration, ρ is density while ρ_0
311 is a reference density, so that $b = -g\rho/\rho_0$ is buoyancy) and

$$312 \quad |\partial U_g / \partial z| = \left| \frac{g}{\rho_0 f} \nabla \rho \right| \quad (11)$$

$$= |\nabla b / f|$$

313 is the magnitude of the thermal wind shear. As said, E is the total eddy energy, i.e. the
314 sum of the EKE and EPE (eddy potential energy). The former is diagnosed using (2)
315 above and the latter from

$$316 \quad EPE = \frac{1}{H} \sum_i \frac{1}{2} \frac{\rho_{i+1} - \rho_i}{\rho_0} g \langle \eta'_{i+1/2} \rangle^2, \quad (12)$$

317 where η' is the height of an isopycnal surface above its mean level. The sum is taken over
318 n density surfaces and, as in all of the above, the prime marks deviations from the zonal
319 mean. Note, finally, that the mixing length diffusivity becomes identical to the GEO-
320 METRIC diffusivity if the mixing length in the former is equal to the ‘Eady scale’, $EKE^{1/2} \sigma_E^{-1}$,
321 and if only EKE is used in the definition of the latter (Wei et al., 2022).

322 Since the work on prognostic eddy energy budgets is still a topic of active research,
323 we set out here to parameterize both the eddy velocity and eddy length scale from coarse-
324 resolution variables. Thus, following Visbeck et al. (1997), we write

$$325 \quad V_{par} \propto \sigma_E L, \quad (13)$$

326 which, moving from proportionality to equality, gives

$$327 \quad K_{par} = a_1 \sigma_E L^2, \quad (14)$$

328 where a_1 is some proportionality constant. Two parameterizations for the eddy length
329 scale are then assessed, namely the WKB-approximation to the internal Rossby defor-
330 mation radius,

$$331 \quad L_R = \frac{\int N dz}{|f|}, \quad (15)$$

332 and the parameterized version of the topographic Rhines scale,

$$333 \quad L_T = \left(\frac{V_{par}}{\beta_T} \right)^{1/2} \quad (16)$$

$$= a_T \frac{\sigma_E}{\beta_T},$$

334 where $\beta_T = (|f|/H)|\nabla H|$ is the topographic beta parameter. Here we have assumed
335 $V_{par} = \sigma_E L_T$ (Eden & Greatbatch, 2008) and introduce a constant tuning factor a_T
336 which may, for example, reflect the resolution of the bathymetric data set used. Figure
337 S2 in the supplementary material shows that in the high-resolution channel model the
338 parameterized L_T (using $a_T = 0.1$) correspond reasonably well with L_T estimate based
339 on diagnosed EKE . Note that equation 16 and the resulting velocity (13) and diffusiv-
340 ity (14) formulations are the same as suggested by Held and Larichev (1996) for poten-
341 tial vorticity diffusivity in beta-plane turbulence, except for their beta being the plan-
342 etary beta. Here parameterized velocity and length scales are always chosen consistently
343 i.e. the parameterized diffusivities will depend on the Eady growth rate and the squared
344 length scale of choice.

345 Finally, topographic impacts on velocity anisotropy and the phase relationship be-
 346 tween velocity and buoyancy perturbations are also diagnosed from the high-resolution
 347 channel simulation. Anisotropy is calculated from (3) while the phase relation is assessed
 348 from the cosine of the angle between the real and imaginary parts of the cross spectrum:

$$349 \quad \cos(\theta) = \frac{\hat{C}o(\bar{v}', \bar{T}')}{\left[\hat{C}o(\bar{v}', \bar{T}')^2 + \hat{Q}u(\bar{v}', \bar{T}')^2 \right]^{1/2}} \quad (17)$$

350 where $\hat{C}o(\bar{v}', \bar{T}')$ and $\hat{Q}u(\bar{v}', \bar{T}')$ are the real and imaginary parts of the cross spectrum,
 351 respectively (the co-spectrum and quadrature spectrum). For analysis, we average θ across
 352 all wavenumbers (k) and over time before calculating the cosine.

353 **3 Eddy fluxes in a channel model**

354 **3.1 Equilibrated flow field and eddy fluxes**

355 Our setup (see section 2.1) is very similar to the setup in the series of papers by
 356 Wang and Stewart (2018, 2020), Wei and Wang (2021), and Wei et al. (2022), except that
 357 we now have continental slopes on both sides of the channel. The forcing is also slightly
 358 different as we employ a westward wind stress which, unlike in the previous studies, is
 359 kept constant across the channel. The mean ocean state, however, is very similar. Since
 360 the channel is in the northern hemisphere, the westward wind stress sets up a northward
 361 surface Ekman transport. Thus, Ekman divergence in the south and convergence in the
 362 north results in a time-mean sea surface tilt which is in geostrophic balance with a west-
 363 ward mean flow, as shown in the two upper panels of Figure 1. The Ekman-driven over-
 364 turning circulation in the y - z plane lifts up isopycnals in the south so that they slope with
 365 the bathymetry there. Conversely, downwelling in the north sets up isopycnals that slope
 366 against the topography.

367 Despite the simple wind forcing, the total baroclinic velocity field is rather com-
 368 plex (Fig. 1a, black dashed lines). In the north there is a strong westward jet over the
 369 slope. This jet has a significant thermal wind shear but nonetheless extends all the way
 370 to the bottom. Over the southern slope the westward flow is weaker and much more surface-
 371 trapped. Lower layers here are almost motionless, so the depth-averaged westward flow
 372 takes on a minimum over the slope (Fig. 1b). Instead there is a broad and nearly barotropic
 373 westward current which has its maximum strength immediately off the seaward side of
 374 the continental slope.

375 The north-south asymmetry is clearly not only a result of the stratification being
 376 weaker in the south than in the north. Thus, net impacts of mesoscale eddy fluxes must
 377 be taken into account. At the most basic level, the tilted isopycnals in both regions are
 378 baroclinically unstable, creating an eddy field whose residual mass transport will tend
 379 to counter the Ekman-driven overturning circulation. However, because mesoscale ed-
 380 dies also transport momentum, the mean flow field reflects, in part, the integrated ef-
 381 fects of eddy momentum and buoyancy fluxes. Their combined effects can be studied in
 382 the Transformed Eulerian Mean (TEM) version of the zonally-averaged zonal momen-
 383 tum equation:

$$384 \quad \frac{\partial \langle u \rangle}{\partial t} - f \langle v^* \rangle = \nabla_{yz} \cdot \mathbf{F}_{EP} + \frac{\partial \langle \tau^x \rangle}{\partial z}, \quad (18)$$

385 where τ^x is the zonal wind stress and

$$386 \quad \mathbf{F}_{EP} = -\langle v' u' \rangle \hat{\mathbf{j}} + f \frac{\langle v' b' \rangle}{N^2} \hat{\mathbf{k}} \quad (19)$$

387 is the Eliassen-Palm (E-P) flux. It consists of a meridional eddy flux of negative u -momentum
 388 and an eddy form stress (this term arises after thickness-weighting). In (18) we have ne-
 389 glected small terms describing the transport of zonal mean momentum by the meridional

390 mean flow as well as vertical flux of momentum (see Wang & Stewart, 2018). Note, how-
 391 ever, that the eddy form stress term, which is connected to lateral buoyancy transport
 392 under the small-slope approximation, may be thought of as a vertical momentum flux.
 393 Finally, the Coriolis term contains the *residual* meridional velocity v^* , i.e. the equiva-
 394 lent mass transport velocity which accounts for both the Eulerian-mean flow and the mass
 395 transport by eddy correlations.

396 The E-P flux from the high resolution experiment 3 (Table 2) is shown as arrows
 397 in the top panel of Figure 1 and its horizontal component (i.e. $-\langle v'u' \rangle$) is shown with
 398 background shading. So what we see is the direction at which the eddy field transports
 399 the westward momentum originally provided by the wind. In general, both in the south
 400 and in the north, the downward eddy momentum flux is suppressed over the slopes, in
 401 agreement with earlier studies which indicate that baroclinic instability of suppressed
 402 over continental slopes. Our estimate of the depth-averaged cross-channel buoyancy dif-
 403 fusivity reflects this signature by being reduced by about two orders of magnitude over
 404 the continental slopes (lower panel). What these simulations show, as also seen in the
 405 simulations of Wang and Stewart (2018) and Manucharyan and Isachsen (2019), is that
 406 eddy motions instead bring zonal momentum laterally across the slopes near the surface
 407 and dump it where the ocean bottom flattens off towards the deep basin. There, over
 408 the relatively flat bottom, baroclinic instability kicks in to bring the momentum down
 409 to the solid ground below.

410 As lateral eddy momentum fluxes are also clearly important in this and previous
 411 simulations, optimal parameterizations will likely need to be build up around down-gradient
 412 PV fluxes (see e.g. Wang & Stewart, 2018). However, it is also reasonable to expect that
 413 any framework which is successful at reproducing the order-of-magnitude drop in buoy-
 414 ancy diffusivities seen in Figure 1 will also improve the ocean state in coarse-grained mod-
 415 els. So we keep this focus here. Hence, on our way towards a practical parameterization
 416 of a GM diffusivity over continental slopes, we begin by examining the length scales and
 417 velocity scales associated with the mesoscale eddy field. This approach is motivated by
 418 the mixing length argument (Prandtl, 1925), relating diffusivity to an eddy velocity scale
 419 and a length scale. However, we will also compare this approach with the energy-based
 420 GEOMETRIC framework (Marshall et al., 2012; Mak et al., 2018).

421 3.2 Eddy length and velocity scales

422 Estimates of eddy length and velocity scales are shown in Figure 2. The length scale
 423 is estimated from (6), i.e. by calculating a spectral-weighted mean wavelength associated
 424 with north-south velocity perturbations. When normalized by its mean value across the
 425 channel the length scale shows a near-universal shape across the various model runs (up-
 426 per left panel). There is a broad maximum over the mid-basin before length scales drop
 427 over the continental slopes on both sides. There is, however, a consistent local maximum
 428 over mid-slope on the northern (prograde) side, coinciding with the maximum in mean
 429 zonal velocity (Fig. 1). Scales then flatten out or even increase over the shelf regions. As
 430 with other diagnostics below, we will largely ignore shelf values from the discussion due
 431 to the model grid not fully resolving the deformation radius there and due to the prox-
 432 imity to model walls. For the eddy velocity scale we show the square root of depth-averaged
 433 EKE. When normalized with the across-channel average (upper right panel), the eddy
 434 velocity scale in all runs is reduced over the southern slope, save for a slight increase over
 435 the upper parts of the slope. In stark contrast, the northern slope is dominated by a large
 436 maximum, also that one centered over the upper parts of the slope. The eddy velocity
 437 then drops off and flattens out over both shelf regions.

438 It would seem that forming a diffusivity from the product of these diagnosed length
 439 and velocity scales may reproduce the observed reduction over the southern retrograde
 440 slope (Fig. 1), at least qualitatively. But it should also be clear that this procedure would

441 produce a diffusivity maximum over the northern slope—for which there is absolutely
 442 no indication in the model fields. We will return to this issue below but first examine
 443 possible scaling approximations to the observed length and velocity scales.

444 We start by comparing the diagnosed L and V with the classical Stone (1972) pre-
 445 diction. So the diagnosed length scale is normalized by the internal deformation radius
 446 L_R (15) and the diagnosed velocity scale is normalized by the product of the Eady growth
 447 rate (8) and the deformation radius, so $V_{scaled} = \sigma_E L_R$. Leaving out any constant pref-
 448 actors here, we see that both length scales and velocity scales are well represented by
 449 Stone-type scaling in the mid-basin (middle panels). The normalized length scales then
 450 drop slightly over the lower parts of both slopes, indicating that the deformation radius
 451 overestimates scales there somewhat. Finally, there is a dramatic rise in normalized scales
 452 over the upper parts of both slopes as the deformation radius drops towards the shal-
 453 low shelves. As with length scales, the normalized velocities drop over the lower parts
 454 of the slopes before rising again over the upper parts. The normalization brings the EKE
 455 peak over the upper parts of the slope down to values similar to those seen over the mid-
 456 basin, as the EKE peak there coincides with the region of stronger thermal shear.

457 Finally, following the suggestion by (Eden, 2007) and (Jansen et al., 2015), we nor-
 458 malize by selecting a smooth minimum of length scales:

$$459 \quad L_{min} = \frac{L_R L_T}{L_R + L_T}, \quad (20)$$

460 where L_T is the topographic Rhines scale (16). The results are similar over the central
 461 basin since the deformation radius is the smaller of the two scales there (the Rhines scale
 462 blows up). But now both normalized length and velocity scales peak over the slopes where
 463 the Rhines scale becomes the smaller of the two—and is quite clearly too small to ex-
 464 plain the observed fields. As such, consideration of the topographic Rhines scale does
 465 not seem to bring any improvement in skill in predicting eddy length scales and veloc-
 466 ity scales over the continental slopes.

467 But before rejecting this scaling choice it is worth noting again that the construc-
 468 tion of a diffusivity from the original (non-normalized) length and velocity scale estimates
 469 would obviously result in a diffusivity maximum over the central northern slope. Such
 470 a maximum is in no way suggested from Figure 1. What may be missing from the story
 471 here is a consideration of how eddy velocity anisotropy and the velocity-temperature phase
 472 relationship may act to bring diffusivities down over the slopes. So we turn to this is-
 473 sue next.

474 3.3 Anisotropy and phase relationship

475 Figure 3 shows the eddy velocity anisotropy A (3) and the cosine of the phase an-
 476 gle between real and imaginary parts of the \bar{v}' and \bar{T}' cross-spectra (17). As expected,
 477 the eddy velocity field is close to being isotropic in the middle of the basin (upper panel).
 478 Values there are around 0.6, implying that cross-channel velocity fluctuations \bar{v}' are in
 479 fact slightly larger than along-channel fluctuations \bar{u}' . The eddy fluctuations then be-
 480 come much more anisotropic towards the continental slopes, with A values over the up-
 481 per parts of the slope close to 0.1 (0.2) in the north (south). This implies that \bar{v}' is about
 482 70% (50%) smaller than \bar{u}' in the north (south). A notable exception is a peak over the
 483 center of the northern slope where \bar{v}' is about 50% larger than \bar{u}' . We have also tested
 484 other measures of anisotropy, such as the velocity based measure used by K. Stewart et
 485 al. (2015) that takes rotational aspects into account, and the results are similar to those
 486 shown here.

487 The general behavior of increased anisotropy over the slopes, with $|\bar{v}'| < |\bar{u}'|$, will
 488 work to reduce the scale-based diffusivity there. But the variations in A from mid-basin
 489 values are not great and the mid-slope peak (where $|\bar{v}'| > |\bar{u}'|$) would actually increase

the estimates there. So we conclude from this that velocity anisotropy alone can not explain the consistent drop in diffusivity by two orders of magnitude over the slopes seen in Figure 1. The phase relation, however, is able to explain the observed order-of-magnitude drop over the slopes, as the \bar{v}' and \bar{T}' fields are close to 90° out of phase there (middle panel). Importantly, the low phase agreement over the northern slope largely cancels the local peak in anisotropy.

The lower panel in Figure 3 shows the product of A and $\cos(\theta)$ (blue lines), an indication of their combined effect. The total suppression is dominated by the information carried in the phase relationship, and velocity anisotropy primarily plays a role near the edges of the two slopes. The suppression over the slopes amounts to more than an order of magnitude, so it is an effect which clearly needs to be parameterized.

The slope-dependent prefactors which previous studies have needed to invoke to explain buoyancy diffusion in similar channel simulations are, in effect, attempts at such parameterization (Brink, 2012, 2016; Hetland, 2017; Wang & Stewart, 2020; Wei et al., 2022). However, at this point we temporarily detour from those earlier studies and instead take as a starting point an expression which bears some resemblance to the final form of the mean-flow suppression factor proposed by Ferrari and Nikurashin (2010). Thus, we construct an ‘eddy efficiency’ factor as

$$E_{eff} = \frac{1}{1 + a_2 (U_{bc}^2/V^2)}. \quad (21)$$

Here, U_{bc} is the large-scale baroclinic flow speed obtained after subtracting the depth-averaged velocity, V is the eddy velocity scale and a_2 is an additional scaling factor which we here take to be constant. The expression does not have a rigorous basis but a simple intuitive interpretation. U_{bc} is directly related to the thermal wind shear and, hence, to the underlying energy source of baroclinic instability (e.g. Sutyrin et al., 2021). Qualitatively, if U_{bc} is large and the flow is baroclinically unstable, one would expect V to be relatively large, giving $E_{eff} \sim O(1)$ (unless a_2 is very large). But if V remains small despite large U_{bc} , some dynamical constraints must be reducing the efficiency of baroclinic energy conversion, implying $E_{eff} \ll 1$. The above interpretation hinges on the parameterized V being an adequate approximation of the actual eddy velocity scale.

We evaluate (21) at each depth but then take the mean over the water column. The large-scale baroclinic flow U_{bc} is extracted directly from the resolved (and zonally-averaged) velocity field, while the eddy velocity is parameterized from (13). The lower panel of Figure 3 shows the resulting efficiency factor, using L_{min} as length scale. The prefactor a_2 has been manually tuned to match the mid-basin values of $A \cdot \cos(\theta)$, but it is clear that using $L = L_T$ can produce a suppression over the continental slope which is in qualitative agreement with $A \cdot \cos(\theta)$ over both slopes for a range of different simulations. Allowing for another prefactor in front of the whole expression (effectively our a_1 parameter) would enable a good quantitative match both over the mid-basin and the slope regions. In contrast, the comparison clearly shows that using L_R as length scale does not reproduce the needed behavior over the slopes. We note that several tests with using the thermal wind instead of U_{bc} and with evaluating (21) with depth averaged-quantities (instead of taking the mean of a depth dependent expression) all produce similar results. Here we chose to use U_{bc} due to the ease of implementation at coarse resolution.

3.4 Parameterized diffusivity

Given the above results, we proceed to examine parameterizations of the diagnosed buoyancy diffusivity. The aim is to capture the order-of-magnitude reduction in diffusivities from the mid-basin to the slope regions. The results are shown in Figure 4 where we distinguish between partial parameterizations (panels a–c) and full parameterizations (panels d–f). The partial parameterizations include extensive information about the mesoscale field itself (such as EKE and L_S) which would not be directly available in a coarse-resolution

540 model, whereas the full parameterizations only use information of the zonally and temporally-
 541 averaged background buoyancy field, Coriolis frequency, and topographic beta, and are
 542 therefore suitable for direct implementation in any existing coarse-resolution model. The
 543 one exception is an estimate (VII) which combines diagnosed EKE with a parameter-
 544 ized length scale. Panels a and d are from one single simulation, showing both the ac-
 545 tual depth-averaged diffusivity diagnosed (black line) and the various approximations
 546 (distinguished by Roman numerals and color). Panels b–c and e–f then show statistics
 547 over both slope regions collected over the whole range of simulations.

548 A first thing to notice from the partial parameterizations is that the mixing length
 549 (I) and GEOMETRIC (II) approaches behave nearly identically. This suggests that i)
 550 EKE and EPE are proportional to each other, as found in the simulations of Wei et al.
 551 (2022), and ii) that our diagnosed eddy scale, L_S , reflects the ‘Eady scale’ $L_E = \sqrt{EKE}\sigma_E^{-1}$
 552 (Larichev & Held, 1995; Jansen et al., 2015; Kong & Jansen, 2021). As also noted by Wang
 553 and Stewart (2020), both approaches thus give reduced diffusivities over the southern
 554 retrograde slope (squared Pearson correlation coefficient r^2 is 0.49 and 0.66, for I and
 555 II, respectively; note that $r = \text{cov}(x, y)/(\sigma_x\sigma_y)$). But the reduction is still underesti-
 556 mated by up to one order of magnitude and reflected as a large relative error. More im-
 557 portantly, over the prograde slope in the north, both approaches result in a serious qual-
 558 itative mismatch, as the high EKE and EPE levels there (EKE seen in Fig. 2; EPE not
 559 shown) produce a non-existing diffusivity peak over mid-slope. Although σ_E also peaks
 560 over the northern slope (not shown), this is not enough to pull down K_{GEOM} there. We
 561 note that the peak in K_{GEOM} over the southern shelf might be spurious as the defor-
 562 mation radius is not well resolved there, which is why we have left the shelves out of this
 563 analysis.

564 The observed discrepancies, particularly the qualitative mismatch over the north-
 565 ern slope, confirms that scaling arguments alone are unable to reproduce the diagnosed
 566 diffusivities—even with knowledge of eddy energy levels and eddy sizes. It is worth not-
 567 ing that this is in line with previous studies (e.g. Wang & Stewart, 2020; Wei et al., 2022)
 568 who found that such scaling estimates needed to be multiplied by slope-dependent pref-
 569 actors to align with diagnosed diffusivities. Here, we instead explicitly examine the role
 570 of velocity anisotropy and the velocity-temperature perturbation phase relationship. Ac-
 571 counting for the diagnosed velocity anisotropy, so that \sqrt{EKE} will be replaced with v'
 572 (III), improves the mixing length estimate slightly but not nearly enough. Multiplying
 573 the two estimates by $A \cos \theta$, however, largely removes the diffusivity peak in the north
 574 and even produces a clear suppression over the slope—for both the mixing length and
 575 GEOMETRIC estimate (IV and V). The values are still higher than the observed dif-
 576 fusivity (mean absolute relative error stays above 100%) but r^2 increases to 0.71 and 0.77
 577 for (IV) and (V), respectively. Over the retrograde slope in the south the match is even
 578 closer, with r^2 reaching 0.92 and 0.85 for (IV) and (V), respectively.

579 Guided by the observed agreement between the mixing length and GEOMETRIC
 580 estimates above, we focus on the former approach when examining how well full param-
 581 eterizations can do. So we assume that a diffusivity can be written as the Eady growth
 582 rate times the square of a length scale. Including our efficiency factor, the effective dif-
 583 fusivity becomes

$$584 \quad K = a_1 \frac{K_0}{1 + a_2 (U_{bc}^2/V^2)}, \quad (22)$$

585 where $K_0 = \sigma_E L^2$ is the scaling estimate of diffusivity before considering the efficiency
 586 factor and where, as discussed above, we have a choice to make for the length scale. For
 587 the constant parameters, we chose $a_1 = 0.25$ so that mid-basin values of VI closely match
 588 with the diagnosed diffusivities across all cases, and we use the same a_1 for (VIII) and
 589 (IX), whereas for (VII) we use $a_1 = 0.66$. Coefficients a_2 and a_T are then tuned man-
 590 ually such that the correlation between the diagnosed diffusivities and estimates (VIII)
 591 and (IX) over the slopes (Fig. 4f) is maximized across all cases.

592 We start by looking at K_0 first. Using the traditional Stone (1972) expression where
 593 the length scale is taken to be the internal deformation radius everywhere, seriously over-
 594 estimates diffusivities over both slope regions (VI). The estimate, in fact, bears some re-
 595 semblance with both the mixing length and GEOMETRIC estimates based on diagnosed
 596 eddy quantities (I and II), but with even larger discrepancies over the slope regions.

597 Switching temporarily to a hybrid estimate, with a diagnosed velocity scale but a
 598 mixing length set to be the smooth minimum of the deformation radius and the param-
 599 eterized topographic Rhines scale (VII; $a_T = 0.5$), improves the skill considerably, giv-
 600 ing in suppressed diffusivities over both slopes. We note that over the slopes, where L_T
 601 is selected, the diffusivity estimate is essentially a topographic version of the Rhines-based
 602 estimate tested by Jansen et al. (2015). They too found that this scaling (with plane-
 603 tary rather than topographic beta) reproduced diagnosed diffusivities well in an two-layer
 604 channel model. Interestingly, in our simulations the skill of this hybrid parameterization
 605 is better than both estimates using full eddy quantities (I and II). Our interpretation is
 606 that our parameterized L_T is a better estimate of the eddy mixing length than the di-
 607 agnosed eddy size L_S (which, from the close correspondence between I and II must re-
 608 flect the Eady scale L_E).

609 Finally, using the full parameterization with Eady growth rate and the minimum
 610 length scale squared (VIII) leads to further improvements over the slopes where the pa-
 611 rameterized diffusivities now drop by nearly two orders of magnitude, approaching the
 612 behavior of the diagnosed diffusivities. Multiplying this estimate with the parameter-
 613 ized efficiency factor (IX) improves the match somewhat over both slopes, especially in
 614 terms of the mean absolute relative error, which drops from 215% (70%) to 116% (53%)
 615 while r^2 increases from 0.73 (0.62) to 0.79 (0.64) over the southern (northern) slope. We
 616 note that across all parameterizations the correlation is higher over the southern slope
 617 than the northern slope, whereas the relative error shows the opposite pattern. This in-
 618 dicates that if one would further tune a_1 , it would be possible to further reduce the re-
 619 lative error metric, especially over the southern slope. However, here, for simplicity, we
 620 chose a_1 such that the diagnosed and parameterized diffusivities match in the central basin.
 621 We also note (not shown) that scaling by E_{eff} improves the hybrid estimate (VI) such
 622 that its performance becomes similar to estimate (IX).

623 A summary of these findings is in order. The parameterized eddy velocity scale and
 624 eddy mixing length, whether based on L_R or L_T , do not reproduce their diagnosed coun-
 625 terparts (\sqrt{EKE} and L_S) over the continental slopes, as seen from Figure 2. But the
 626 failure of diagnosed eddy energy and L_S in predicting a diffusivity over the slopes, par-
 627 ticularly over the prograde slope in the north, also indicates that these eddy quantities
 628 do not give the full story. In particular, the eddy scale—which also appears to be related
 629 to EKE via the Eady length scale $L_E = EKE^{1/2}\sigma_E^{-1}$ —is not a good predictor of the
 630 effective mixing length. Accounting for the phase relationship between eddy velocity and
 631 buoyancy perturbations and, to a lesser degree, the eddy anisotropy brings the estimates
 632 much closer to the actual diffusivity. Our attempts at full parameterizations then clearly
 633 shows that L_T is a much better choice than L_R over both continental slopes. And the
 634 comparison between estimates VII and VIII even suggests that $V_{par,T} \propto \sigma_E^2/\beta_T$ is a
 635 slightly better predictor for the effective eddy mixing velocity over the slopes than the
 636 square root of eddy kinetic energy. Thus, a further consequence appears to be that the
 637 need for an explicit suppression factor (our E_{eff}) for the fully parameterized diffusiv-
 638 ity becomes smaller. We leave further examination of this topic for later and instead carry
 639 on to see what effects the parameterized expression (IX) will have when used to actu-
 640 ally operate in coarse-grained, non-eddy, simulations.

641

3.5 Performance in a coarse-resolution channel simulation

642

643

644

645

646

647

648

649

Before moving to realistic global simulations, we test the proposed parameterizations in a coarse-resolution channel setup. This setup has the same geometry as the high-resolution channel setup, but differs in resolution (from 2 km to 32 km) and in that the the GM-Redi parameterization scheme is activated. The model is forced and run similarly to the high-resolution setup, but some parameter settings, such as timestep and viscosity, are necessarily modified. Acknowledging that the channel setup is quite specific, and in anticipation of the global simulations to be studied next, we have kept tuning of the coarse-resolution channel setup to a minimum.

650

651

652

653

654

655

656

657

658

659

660

661

662

663

664

665

666

667

668

Figure 5 shows parameterized buoyancy diffusivities and the time-mean density field in three of the equilibrated simulations that had wide continental slopes but differing initial stratification. We chose to use the wide continental slope case because that is best resolved at 32 km resolution. We also show the corresponding diagnosed quantities from the corresponding high-resolution simulations for comparison (black lines). As in Figure 4, we show the three versions of the parameterized diffusivity (and corresponding density structure): one using the internal deformation scale (with $a_1 = 8$), one using the minimum between internal deformation scale and topographic Rhines scale (with $a_1 = 8$ and $a_T = 0.1$) and, finally, one using the minimum and also applying the parameterized eddy efficiency factor (with $a_1 = 32$, $a_2 = 1$, and $a_T = 0.1$). Choosing $a_T = 0.1$ is consistent with the high-resolution model diagnostics as it provides a reasonable fit in terms of the order of magnitude between the full and parameterized versions of the topographic Rhines scale (see Figure S2 in supplementary material). Together, constants a_1 and a_T scale the diffusivity estimate by 0.08 (without E_{eff}) and 0.32 (with E_{eff}) over the sloping regions. These appear similar to the scaling coefficients used in Figure 4 (~ 0.25 , see figure caption) as well as previously reported values with mixing length theory: 0.33 by Wang and Stewart (2018) and 0.17 by Wei et al. (2022), both focusing on buoyancy diffusivity, as well as 0.2 by Wei and Wang (2021), although they focused on along isopycnal diffusivity.

669

670

671

672

673

674

675

676

677

678

679

680

681

682

683

The tuning of a_1 was done to approximately match the mid-basin parameterized diffusivity with the corresponding diagnosed diffusivity in the high-resolution simulations. And yet, Figure 5 shows that the parameterized diffusivities have a clear north-south gradient in the magnitude whereas their diagnosed counterpart does not (panels a-c). The discrepancy is caused by a stronger difference in stratification between north and south at coarse resolution (see Figure S3 in the supplementary material) which directly impacts the internal deformation radius used by the parameterization over the central flat region. Despite this, we push forward and review the performance of the different parameterizations over the continental slopes. The deformation scale-based parameterization (Fig. 5a-c, orange line) clearly does worst, producing local diffusivity maxima over both slopes, as also seen in Figure 4 (blue line). Thus, there are only very weak lateral density fronts, or thermal wind shears, over the continental slopes. Essentially, the high parameterized diffusivities effectively wash out any density front there (see Fig. 5d-f for density structure and Fig. S3 for the density gradients). This, it should be remembered, is exactly the effect one wishes to reduce with a slope-sensitive parameterization.

684

685

686

687

688

689

690

691

692

693

The run using a parameterization which selects the minimum of the two length scales does much better over both continental slopes where the topographic Rhines scale kicks in. With suppressed diffusivities, the density front which is set up by the topographic PV gradient is no longer washed out completely, especially in the north (see Fig. 5g-l for density structure and Fig. S3 for the density gradients). The result is an enhanced thermal wind shear over the northern slope, albeit with a lower absolute strength than in the high-resolution simulation (about a factor two lower). In the south, where the vertical stratification is much weaker, the parameterization is not able to set up a strong thermal wind shear, although the location and strength of the surface density front has improved. Further scaling by the eddy efficiency E_{eff} (Fig. 5, green) enhances the dif-

694 fusivity reduction slightly in the north, but not necessarily in the south. Therefore, the
 695 feedback to the resolved fields strengthens the baroclinic jet in the north further, but not
 696 in the south.

697 Clearly, there remains significant discrepancies between the low-resolution and high-
 698 resolution fields. Some may be due to higher levels of implicit (numerical) diffusion in
 699 the coarse-resolution simulations, but others likely reflect limitations in the parameter-
 700 ization. More extensive tuning, e.g. based on matching the baroclinic transport over the
 701 slopes, would likely bring the coarse resolution simulations closer to the high-resolution
 702 fields. But the aim here has primarily been a qualitative examination, and even with a
 703 minimum of tuning the behavior over the slopes is robust, as the response to the differ-
 704 ent parameterizations is consistent across all cases. All in all, the above results are en-
 705 couraging in that the Rhines-based parameterization is able to reduce wash-out of the
 706 density fronts over the slopes—particularly over the prograde slope in the north. How-
 707 ever, although the channel setup is a reasonable test bed for development, it is extremely
 708 idealized and lacks multiple features from the real world (e.g. variable Coriolis param-
 709 eter, uneven topography and complex atmospheric forcing). Therefore, we also test the
 710 slope-aware parameterization in the realistic global domain next.

711 4 Realistic global model simulations

712 4.1 Eddy parameterization adjustments

713 We carry out a control simulation and 5 different perturbation experiments. For
 714 simplicity, the focus will mostly be on a comparison between the control simulation and
 715 two of the perturbation experiments. All of these simulations operate with 2D diffusiv-
 716 ities based on the depth-averaged Eady growth rate and a square length scale, as in (14).
 717 The control run selects a length scale from the minimum of the internal deformation ra-
 718 dius and the planetary Rhines scale (not the topographic Rhines scale). Then, in two
 719 distinct ‘topo’ runs we i) introduce the topographic Rhines scale as an additional length
 720 scale and ii) also turn on the eddy efficiency factor E_{eff} . The OMIP ‘topo’ runs then
 721 differ slightly from the coarse-resolution channel setup in the choice of constant scaling
 722 factors. The constant factor a_1 which scales the overall diffusivity magnitude is set to
 723 3 and factor a_2 used in E_{eff} is set to 1. In addition, we adjust L_T by trying $a_T = 1$
 724 and $a_T = 0.5$. We view these constants as tuning factors specific to one particular setup;
 725 for example, a_T is impacted both by the quality of the parameterized Rhines scale (Fig.
 726 S2) as well as the bottom topography dataset. Here we calculated the topographic beta
 727 parameter based on the model’s bathymetry. An improved approach might be to take
 728 a high-resolution bathymetry product and low-pass filter it up to the mesoscale—e.g. to
 729 the deformation radius or slightly above—before calculating the slopes. Further anal-
 730 ysis is left for future studies, but in Figure S1 (supplementary material) we show that
 731 the model bathymetry-based β_T is a reasonable fit to high resolution bathymetry-based
 732 β_T (using 15 second resolution bathymetry by Sandwell et al., 2022) after filtering to the
 733 local deformation radius. Finally, in all runs the diffusivity magnitude is scaled down with
 734 a resolution function (Hallberg, 2013) when the deformation radius is resolved by the
 735 model grid.

736 For simplicity, the along-isopycnal (Redi) tracer diffusivity is set to be the same
 737 as the GM diffusivity. We have assessed the impact of this choice in a set of additional
 738 experiment included in the supplementary material (Fig. S4) and summarized the find-
 739 ings in section 4.2.

740 To put the OMIP experiments in some context, it should be mentioned that the
 741 model settings for the control run are similar to the NorESM model version used in the
 742 latest Climate Model Intercomparison Project (CMIP6) except for some aspects of the
 743 GM diffusivity formulation. The CMIP6 version of the model included a mixing length

744 formulation where the length scale was selected as the minimum of the internal defor-
 745 mation radius and the planetary Rhines scale—as in our control simulation. However,
 746 the local Eady growth rate was then evaluated at each model level, rendering a 3D pro-
 747 file for both eddy driven advection (GM) and for along isopycnal mixing (Redi). Finally,
 748 the scaling-based diffusivity was adjusted by a zonal velocity-dependent mean flow sup-
 749 pression following Ferrari and Nikurashin (2010), and as in the experiments here, a res-
 750 olution function (Hallberg, 2013) was also used.

751 The lack of vertical structure of the 2D parameterization proposed here, turned out
 752 to be a clear deficiency in the global domain as our initial simulations showed an unre-
 753 alistically strong sensitivity to bottom slopes in the low and mid-latitude deep ocean.
 754 For example, large reductions in the parameterized diffusivity across mid-ocean ridges
 755 were not seen in eddy-permitting studies that diagnosed eddy diffusivity in the global
 756 domain (e.g., Bachman et al., 2020). Therefore, to reduce the topographic impact on eddy
 757 fluxes in strongly stratified low and mid-latitude regions, we added an ad hoc ‘limiter’
 758 of topographic effects—based on the assumption that if the resolved flow does not feel
 759 the bottom then it is unlikely that mesoscale eddies would do so either. Specifically, the
 760 topographic Rhines scale is scaled by $\cos(\alpha)^{-10}$ which rapidly increases the topographic
 761 Rhines scale when the angle α between the resolved depth-averaged flow and the bot-
 762 tom slope tangent vector deviate by more than $\sim 30^\circ$ i.e. when the resolved depth-averaged
 763 flow is not aligned with the bottom slope.

764 4.2 Model response in the global domain

765 As expected, introducing the topographic Rhines scale leads to locally reduced dif-
 766 fusivities over sloping topography, as shown in Figure 6 (top row). The effect is enhanced
 767 at high latitudes with a $\sim 50\%$ reduction over Arctic and Antarctic continental slopes.
 768 Bringing in the eddy efficiency E_{eff} (see Figure S6 and text S6 in the supporting infor-
 769 mation for an estimate of the E_{eff} pattern) leads to additional and more severe diffu-
 770 sivity reduction globally, also away from topographic features (bottom row). This is also
 771 in agreement with recent studies (admittedly focusing on Redi mixing) that found that,
 772 at large scales, the scaling by mean-flow dependent suppression has the largest impact
 773 on diffusivity (Stanley et al., 2020; W. Zhang & Wolfe, 2022; Holmes et al., 2022). Note
 774 that in the tropics, the diffusivity is limited by the grid resolution function (Hallberg,
 775 2013), i.e. the diffusivity is reduced when the grid size is smaller than the local defor-
 776 mation radius. Therefore, the large relative reduction in tropical diffusivity is small in
 777 absolute terms and less important there as transport is dominated by the resolved flow.
 778 Finally, we note that a comparison between the top and the bottom rows in Figure 6 shows
 779 that in multiple continental slope regions, especially in the Arctic and around Antarc-
 780 tica, the eddy efficiency simply enhances the response seen with the topographic Rhine
 781 scale. Indeed, the diffusivity reduction due to introducing the topographic Rhines scale
 782 and due to eddy efficiency are close to linearly additive (not shown).

783 As the impact of eddy efficiency on diffusivity is more broad, its impact on flow speed,
 784 temperature, and salinity is also more widespread than the impact of the topographic
 785 Rhines scale alone. Table 3 collects bias reductions (relative to the control case) across
 786 5 different experiments while Figures 7–9 show the spatial patterns for subsurface (100–
 787 200 m) current speed and temperature, as well as zonal-mean temperature and zonally-
 788 integrated overturning streamfunction anomalies for the two ‘topo’ experiments that are
 789 in focus here (the overturning volume streamfunction is diagnosed by dividing the online-
 790 calculated overturning mass streamfunction with a constant reference density, $\rho_0 = 1000$
 791 kg m^{-3}). We show results for the subsurface response since the surface response in these
 792 forced simulations is strongly forced by the non-responsive atmosphere. Both the topo-
 793 graphic Rhines scale alone and its combination with eddy efficiency increase the mean
 794 kinetic energy of the resolved flow globally (at 100–200 m depth, by 2.7% and 10.5%,
 795 respectively). This increase is especially noticeable over sloping bathymetry where the

796 two impacts contribute approximately equally to the overall increase (over slopes where
 797 $\beta_T > 5 \cdot 10^{-10} \text{m}^{-1} \text{s}^{-1}$ kinetic energy at 100–200 m depth increases by 9.1% and 20.8%,
 798 respectively). The two modifications also warm the ocean below the global thermocline
 799 and cool the surface, reducing the overall temperature bias at depth. But they increase
 800 the temperature bias at the thermocline (Table 3; Fig. 9a,c).

801 Overall, the mean overturning response in the ‘topo’ runs is characterized by a posi-
 802 tive (cyclonic) anomaly which implies that the Atlantic overturning cell and the Dea-
 803 con cell in the Southern Ocean strengthen, whereas the Antarctic Bottom Water cell and
 804 the shallow surface overturning cells within the subtropical and subpolar gyres weaken.
 805 These changes generally reduce biases. The simulated strength of the Atlantic overturn-
 806 ing at 26°N is 15.5 Sv in the control simulation, 17 Sv when topographic Rhines scale
 807 is considered, and 18 Sv with the addition of eddy efficiency, whereas the observational
 808 estimate from the RAPID array ($\sim 26^\circ \text{N}$) is 17 ± 3.3 Sv (Frajka-Williams et al., 2019).
 809 The Antarctic bottom water cell at 32°S weakens from 26.0 Sv in the control simulation
 810 to 23.5 Sv with topographic Rhines scale and 20.3 Sv with addition of eddy efficiency,
 811 whereas inverse modelling suggest 20.9 ± 6.7 Sv (Lumpkin & Speer, 2007). The Deacon
 812 cell strengthens from 13.2 Sv in the control simulations to 15.2 Sv with the topographic
 813 Rhines scale and 18.4 Sv when eddy efficiency is considered, whereas previous modelling
 814 estimates (Döös et al., 2008) and observational estimates (Speer et al., 2000) suggest a
 815 strength of 20 Sv and 20–25 Sv, respectively.

816 Some more specific impacts of the topographic Rhines scale and eddy efficiency are
 817 a poleward shift and strengthening of the boundary and slope currents, with E_{eff} gen-
 818 erally speeding up the boundary currents at locations where observations show the core
 819 of the currents (Fig. 7, observed currents in black contours). Changes in the net volume
 820 transports in most key passages remain small (Table 4), but the results show a strength-
 821 ening of the ACC (Drake Passage transport; reduced bias), a general enhancement of wa-
 822 ter exchange between the Arctic and mid-latitudes (opposing influence on the bias in dif-
 823 ferent straits), and strengthening of the Gulf Stream (Florida–Bahamas strait transport,
 824 reduced bias). The spinup of the ACC is a direct consequence of reduced diffusivities,
 825 allowing for stronger thermal wind currents. In the northern North Atlantic, the cur-
 826 rent speed response is directly reflected in the temperature response as the Atlantic Wa-
 827 ter warms up along its path from the Nordic Seas to the Arctic (Fig. 8, reduced bias).
 828 Despite the speed-up of the Gulf Stream off the North American coast, its observed turn-
 829 ing around Grand Banks off Newfoundland is not reproduced. Due to this deficiency, the
 830 cold bias off Newfoundland strengthens (Fig. 8). This cold bias is a long standing issue
 831 in coarse resolution ocean models (Tsujino et al., 2020) and reducing the diffusivity along
 832 the current path or along the shelf break clearly does not mitigate the bias. We spec-
 833 ulate that, similar to the southern retrograde slope in the channel configuration and re-
 834 cent results on the Gulf Stream reported by Uchida et al. (2022), the eddy momentum
 835 flux convergence that is not included in the parameterization plays a crucial role in de-
 836 termining the current path.

837 The overall overturning response leads to increasing heat transport towards the north-
 838 ern hemisphere (Fig. 10). The northern hemisphere subtropical peak in northward heat
 839 transport in the Atlantic basin (globally) is 0.83 PW (1.07 PW) in the control simula-
 840 tion, 0.91 PW (1.15 PW) when topographic Rhines scale is considered, and 1.00 PW (1.26
 841 PW) with the addition of eddy efficiency, whereas Trenberth et al. (2019) estimate ap-
 842 proximately 1.1 PW (1.6 PW). Breaking down the zonally-integrated impacts into re-
 843 solved and parameterized eddy components illustrates how the reduced eddy mass trans-
 844 port across the ACC (Fig. 10, panels a–b) also leads to less southward heat transport
 845 (Fig. 10, panels c–e) and therefore a cooling of the Southern Ocean surface, but also warm-
 846 ing over the continental slopes (Fig. 8). Both these effects reduce the bias in the model.
 847 Note that the heat transport response is dominated by eddy-driven advection with a smaller
 848 contribution due to the eddy diffusion (Fig. 10, panels d–e). In contrast to the South-

ern Ocean, in the northern mid-latitudes the overall northward mass and heat transport increase as the mean overturning spins up (Fig. 10 panels a and c; Fig. 9 right panels) and the eddy contributions actually weaken (Fig. 10, panels b, d-e).

We note again that in these OMIP experiments we have taken the eddy driven advection ('GM') and isopycnal mixing ('Redi') coefficients to be the same, making the origin of the response ambiguous. However, with a set of additional experiments (supplementary material, Figure S4) we show that the circulation response is mostly due to GM and, to a large extent, can be constructed as a sum of experiments where GM and Redi are changed separately (i.e. the response is linearly additive). The detailed temperature response, especially the thermocline bias, is sensitive to the treatment of the along-isopycnal mixing, but here the combined response is not linearly additive. The non-linear temperature response suggest that when developing and tuning a model system the changes to GM and Redi parameterizations should be made simultaneously.

5 Discussion

Our study has focused on a relatively small range of parameterization choices, essentially i) re-examining the topographic Rhines scale as a relevant mixing length and ii) checking the importance of an additional suppression factor which we have called the eddy efficiency E_{eff} . The studies by Wang and Stewart (2020) and Wei et al. (2022) did a more comprehensive sweep over possible parameterization choices but did not analyse prograde and retrograde bottom slopes under one and the same framework, which has been the intention here. Also, to the best of our knowledge, the current OMIP simulations constitute the first assessment of the impacts of a topographically-aware GM parameterization in realistic global ocean models. As such, this work should be taken as a pragmatic investigation into what can be achieved with simple parameterization approaches applied to existing models that do not contain a prognostic eddy energy equation (which in itself requires parameterization choices). As with all parameterizations, the options examined here are far from perfect, and below we discuss some shortcomings and unresolved questions.

5.1 The relevance of the topographic Rhines scale

Earlier idealized model studies have given conflicting evidence for the relevance of the topographic Rhines scale. Jansen et al. (2019) and Kong and Jansen (2021) reported that using a generalized Rhines scale which accounts for both planetary and topographic beta in their eddy parameterization of flows in an idealized ACC-like domain improved their model skill. More in line with our work here, the idealized channel studies of Wang and Stewart (2020) and Wei et al. (2022) found the topographic Rhines scale to be a useful choice over retrograde slopes—but not over prograde slopes. This conclusion was drawn, however, after an empirical slope-dependent prefactor was applied in the retrograde case but not in the prograde case. Both studies also constructed diffusivities from diagnosed depth-averaged EKE . In other words, they set the eddy velocity scale to be $V = \sqrt{EKE}$ and then defined $L_T = \sqrt{V/\beta_T}$, i.e. using the actual definition of the topographic Rhines scale. However, here we find that over both prograde and retrograde slopes, a full parameterization using (14) with $L_T = a_T \sigma_E / \beta_T$, better reproduces diagnosed diffusivities from our high-resolution simulations than partial a parameterization using (5) with $L_T = \sqrt{V/\beta_T}$ (see Fig. 4). Although not analyzed in detail, our hypothesis is that the full parameterization produces better results because it leads to a β_T^{-2} dependence for the overall diffusivity, instead of the $\beta_T^{-1/2}$ dependence when using (5) and the actual definition of L_T . The different power dependence is important because β_T varies by several orders of magnitude across the slopes whereas EKE and σ_E vary by less than one order of magnitude (see e.g Fig. 2).

898

5.2 The interpretation of E_{eff}

899

900

901

902

903

904

905

906

907

908

909

910

911

912

It is worth noting that our E_{eff} may be related to the topographic Eady problem of Blumsack and Gierasch (1972). This connection becomes apparent if we evaluate the 2D version of (21). We begin by setting $U_{bc} = U_{tw}$, where U_{tw} is the top-to-bottom thermal wind shear (a 2D quantity). Then we first consider the slope region where the topographic Rhines scale will be the relevant length scale. So, here, $V = \sigma_E^2/\beta_T$, where σ_E is now the depth-averaged (2D) Eady growth rate. Noting that in the Eady model, where both N^2 and $\partial U_g/\partial z$ are constant, $\sigma_E = 0.3 \cdot U_{tw}/L_R$. This allows us to rewrite (21) as

913

$$\begin{aligned} E_{eff} &= a_1 \frac{1}{1 + a_3 (\beta_T L_R^2 / U_{tw})^2} \\ &= a_1 \frac{1}{1 + a_3 \delta^2}, \end{aligned} \quad (23)$$

914

915

916

917

where a_3 is a modified tuning factor. Here $\delta = \beta_T L_R^2 / U_{tw}$ is the slope parameter of Blumsack and Gierasch (1972) which measures the ratio between topographic and isopycnal slopes. Equation 23 is further supported by Figure S5 (in the supplementary material) showing reasonable correspondence (up to a constant) between U_{bc}^2/V^2 and δ^2 .

918

919

920

921

922

923

924

925

926

927

928

929

930

931

932

This expression is interesting not only because it brings in the controlling parameter of the modified Eady problem but also for its similarity to the slope-dependent prefactor used by Wang and Stewart (2020) over retrograde slopes in the parameter regime where the bottom slope is not much larger than the isopycnal slope. Their prefactor F_{MLT} (from their table 3) has the topographic delta parameter to the power of one in the denominator, in contrast to our squared power. But we suggest that the impact of sampling errors in the empirical fitting be studied in future studies before the correspondence is rejected. We also note that the similar studies of prograde fronts by Brink (2016) and Wei et al. (2022) found best fits using similar expressions but using topographic Burger number Bu in place of the delta parameter, where the two are related via $Bu = (\sigma_E/f) \delta$. The latter study concluded that scalings using δ instead of Bu were not successful over prograde slopes. But, again, a comparison with our results is not straightforward since their diffusivities were constructed using diagnosed EKE while ours are fully parameterized. The relationship between δ -based and Bu -based formulations is also an obvious topic for future work.

933

934

935

936

937

938

939

940

941

942

943

944

945

946

Note, finally, that over the flat regions where the deformation radius will act as the relevant length scale, the 2D version of our efficiency factor becomes constant, in agreement with the behavior seen in Figure 3. In fact, the 2D version of E_{eff} was able to qualitatively reproduce the observed eddy efficiency behaviour in the idealized channel simulations, with some changes required for the tuning constants (not shown). We nonetheless chose to use the 3D version in the realistic OMIP simulations in anticipation of a more complex hydrography and flow field where the various assumptions of the Eady model can be expected to hold to an even lesser degree than in the channel model. Interior thickness PV gradients, for example, are expected to be small in systems that are only forced by Ekman pumping, as our channel model is (see e.g. Meneghello et al., 2021; Manucharyan & Stewart, 2022). In a real ocean, where e.g. thermohaline forcing can produce interior PV gradients, the suppression of eddy efficiency will inevitably be governed by additional non-dimensional parameters beyond Blumsack and Gierasch (1972) δ (or, alternatively, the topographic Burger number). Such 3D effects, caused by thermohaline forcing in ad-

947 dition to wind stress, may also be the underlying reason for why E_{eff} had a much big-
 948 ger impact in the OMIP simulations than it did in the channel.

949 6 Summary and conclusions

950 Efforts to include topographic effects into mesoscale eddy parameterizations are
 951 warranted, especially at high latitudes where observations show that hydrographic fronts
 952 are typically locked to topography. The very existence of such fronts along continental
 953 slopes and submarine ridges imply not merely topographic steering of large-scale cur-
 954 rents but also suppression of lateral mixing across topography. Yet, despite all the ob-
 955 servational evidence, as well as solid theoretical arguments for e.g. reduced growth rates
 956 and length scales of baroclinic instability over sloping topography, most eddy parame-
 957 terizations still do not account for any bathymetric influence.

958 Here we have re-examined the relevance of the topographic Rhines scale in the mix-
 959 ing length approach to parameterizing the Gent-McWilliams buoyancy diffusivity which
 960 is used for eddy advection. Constructing diffusivities using the Eady growth rate and
 961 a parameterized version of the topographic Rhines scale reproduces an observed order-
 962 of-magnitude reduction in diffusivity over continental slopes in idealized channel sim-
 963 ulations. The simulations and analysis cover both prograde and retrograde continental
 964 slopes, representing mean flows in the same and opposite direction to topographic waves,
 965 respectively. Although differing in detail, both the observed and parameterized mixing
 966 suppression are of similar order of magnitude on both sides. The skill of the parameter-
 967 ization is enhanced further, at least over the prograde slope, when the diffusivity is mul-
 968 tiplied by an eddy efficiency factor E_{eff} that is sensitive to the strength of the mean-
 969 flow vertical shear relative to the parameterized eddy velocity scale. Finally, we find that
 970 selecting a smooth minimum of the topographic Rhines scale and the internal deforma-
 971 tion radius for length scale gives good skill over the entire idealized channel domain.

972 The parameterization is then tested in a realistic global ocean simulation. Com-
 973 parison with a simulation where topographic effects on diffusivities are not included sug-
 974 gests that the topography-aware parameterization enhances the sharpness of hydrographic
 975 fronts and, as such, strengthens the thermal wind shear in boundary currents. The im-
 976 provement is particularly noticeable at high latitudes, but we also observe large impacts
 977 throughout the world ocean. The globally-averaged temperature and salinity bias reduc-
 978 tions are in the range $O(1\%)$ – $O(10\%)$, with largest reductions seen in Southern Ocean
 979 temperatures and in Atlantic Water temperatures in the Arctic. However, existing low-
 980 latitude thermocline biases tend to increase.

981 The complex pattern of bias changes seen is not uncommon in a realistic global model,
 982 as bias reduction is very much a tuning exercise involving a range of free parameters as-
 983 sociated with different parameterizations (e.g. eddy transport, vertical mixing and air-
 984 sea-ice fluxes). Our parameterization also has free parameters and, as is common, we found
 985 that the different model configurations, specifically different resolutions, might require
 986 different values for these. But we did not attempt a rigorous tuning, especially not for
 987 the dynamically complex OMIP simulations. Simply put, the focus at this stage has not
 988 been on a well-tuned realistic global simulation, but rather on illustrating possible im-
 989 pacts of a topography-aware eddy parameterization.

990 The suggested parameterization is clearly incomplete. The relatively large differ-
 991 ence in importance of the efficiency factor E_{eff} between the coarse-resolution channel
 992 simulations and the realistic OMIP simulations is one indication of this. A second one
 993 is the fact that we had to use an ad hoc limiter when applying this in the OMIP sim-
 994 ulations. One key reason why a limiter had to be used is likely that we have been ignor-
 995 ing any vertical structure in eddy velocities and, ultimately, diffusivities. Fundamentally,
 996 the kinematic interaction with the bottom involves eddy bottom velocities, and a num-

997 ber of observations as well as theoretical arguments have indicated that these are often
 998 significantly smaller than surface or even depth-averaged eddy velocities (see e.g. Kill-
 999 worth, 1992; Wunsch, 1997; de La Lama et al., 2016; Lacasce, 2017). The topographic
 1000 impact, under such considerations, would probably be smaller than if estimated with depth-
 1001 averaged quantities. Future work clearly needs to be put on such vertical structure, for
 1002 example by taking an equivalent barotropic structure as a starting point (Killworth, 1992).
 1003 We also observe that in our coarse-resolution channel simulations the flow remains too
 1004 baroclinic, similar to the results presented by by Kjellsson and Zanna (2017); Yankovsky
 1005 et al. (2022). Although addition of vertical structure to the buoyancy diffusivity might
 1006 mitigate the issue, feeding the mean flow with vertically-distributed eddy energy (e.g.
 1007 via a backscatter-type parameterizations) might be needed to resolve it (Yankovsky et
 1008 al., 2022).

1009 Another key topic which we have entirely neglected in this study is the impact of
 1010 bottom roughness or corrugations on fluxes—and how such impact may be asymmetric
 1011 with respect to the flow direction. As demonstrated by Wang and Stewart (2020),
 1012 bottom roughness along a retrograde topographic slope can set up additional eddy buoy-
 1013 ancy transport and, thus, form stresses due to arrested topographic waves. The dynam-
 1014 ics governing such fluxes are likely distinct from those captured by our parameterizations
 1015 here for smooth topography. The relevant eddy length scale, for example, is probably
 1016 not the same as for transient eddies (Khani et al., 2019), and even coarse resolution mod-
 1017 els might be able to reproduce some of the largest standing meanders (Kong & Jansen,
 1018 2021). The application of standing Rossby wave theory (e.g. Abernathy & Cessi, 2014;
 1019 A. L. Stewart et al., 2023) appears to give promising results on the planetary beta plane
 1020 with a flat but rough bottom. A natural next step may therefore be to examine such ideas
 1021 to the ‘topographic beta’ problem, using e.g. the idealized two-slope model used here.

1022 Yet another issue ignored here is the role of lateral eddy momentum fluxes over con-
 1023 tinental slopes. As shown in Figure 1 and also highlighted in earlier studies (e.g. Wang
 1024 & Stewart, 2018; Manucharyan & Isachsen, 2019), such fluxes bring wind momentum off
 1025 the slopes to relatively flat regions where baroclinic instability kicks in to transfer the
 1026 momentum to the ground below. The lateral momentum flux may be up-gradient in places
 1027 and form eddy-driven jets, as seen offshore of the retrograde slope in our idealized sim-
 1028 ulations (Fig. 1). As with eddy form stress, lateral momentum fluxes also appear to be
 1029 impacted by corrugated bottoms, being associated with the formation of prograde jets
 1030 near the bottom (Wang & Stewart, 2020). This last effect is again probably related to
 1031 the formation of arrested topographic waves, as discussed by e.g. Haidvogel and Brink
 1032 (1986), as well as being linked to down-gradient PV diffusion in the finite-amplitude limit
 1033 (Bretherton & Haidvogel, 1976; Vallis & Maltrud, 1993).

1034 Finally, it’s worth remembering that eddy transport, even of buoyancy, may be anisotropic.
 1035 So what really needs to be parameterized is a diffusion tensor rather than a single scalar.
 1036 Bachman et al. (2020) discussed such anisotropy of the Redi diffusion tensor and showed
 1037 that at global scale the direction of the major axis of the tensor is well correlated with
 1038 the mean flow direction and the minor axis is well correlated with the gradient of Er-
 1039 tel PV. In addition, Nummelin et al. (2021, Appendix A) suggested that the Ferrari and
 1040 Nikurashin (2010) type of mean-flow suppression indeed suppresses the across-flow Redi
 1041 mixing, but that the inverse of the same factor enhances mixing in the along-flow direc-
 1042 tion. It remains unclear whether our eddy efficiency factor—here primarily applied to
 1043 buoyancy mixing—and the other empirical scaling factors (e.g. Wang & Stewart, 2020;
 1044 Wei et al., 2022) act similarly (i.e. relate to tensor anisotropy) or if they indeed suppress
 1045 the overall tensor magnitude. In other words, it remains a research question whether the
 1046 mean flow and topography merely direct the eddy transport or if they impact the over-
 1047 all magnitude of the eddy transport. Nevertheless, if the tensor major axis is correlated
 1048 with the mean flow (as suggested by Bachman et al., 2020)—and if that mean flow trans-
 1049 port dominates over eddy transport—then the focus on the minor axis is likely justified.

Table 1. BLOM model constants for the channel simulations

Name	Symbol	Value
Wind stress	τ_x	0.05 N m ⁻²
Horiz. grid size	$\Delta x, \Delta y$	2 km
Baroclinic timestep	Δt	120 s
Domain x-size	L_x	416 km
Domain y-size	L_y	1024 km
Gravitational acceleration	g	9.806 m s ⁻²
Coriolis parameter	f_0	1×10^{-4} s ⁻¹
Slope mid-point distance from domain edge	Y_S	150 km
Shelf depth	H_{Shelf}	250 m
Slope height	H_{Slope}	2000 m

Table 2. Key parameters in the various high-resolution channel model experiments. L_R is the mean deformation radius in the central basin (where bottom depth is larger than 2250 m).

Name	L_R	Slope Width
Exp 1	34.1 ± 1.3 km	75 km
Exp 2	34.1 ± 1.1 km	100 km
Exp 3	34.4 ± 1.0 km	125 km
Exp 4	30.6 ± 1.3 km	75 km
Exp 5	30.6 ± 1.2 km	100 km
Exp 6	30.4 ± 1.0 km	125 km
Exp 7	24.9 ± 1.2 km	75 km
Exp 8	25.9 ± 1.0 km	100 km
Exp 9	24.9 ± 1.0 km	125 km

1050 Even if important questions remain, and despite its many shortcomings, the rel-
1051 atively simple parameterization investigated here at least reduces an excessive washing
1052 out of hydrographic fronts over submarine ridges and continental slopes in ocean climate
1053 models—a known problem with eddy parameterizations that are insensitive of bathymetry.
1054 One of several important consequences of such adjustment is likely a more accurate rep-
1055 resentation of oceanic heat transport across Antarctic and Greenland continental slopes
1056 and onward to the great ice sheets whose melt rates depend intimately on such trans-
1057 port. On the shallow continental shelves, tides and other ageostrophic processes which
1058 we have neglected entirely here will also contribute. However, getting fluxes right across
1059 the strong fronts along the continental slopes is no less important. For this and other
1060 reasons, further scrutiny of all of the above unresolved issues related to mesoscale eddy
1061 transport and their impacts in both regional and global realistic simulations are much
1062 needed.

1063 7 Open Research

1064 The model configuration and namelists needed for reproducing the results are pub-
1065 lished in Zenodo (Nummelin, 2023b) and available at [https://doi.org/10.5281/zenodo](https://doi.org/10.5281/zenodo.8227381)
1066 [.8227381](https://doi.org/10.5281/zenodo.8227381). The key model outputs (Nummelin, 2023a) needed for reproducing the anal-
1067 ysis are published at the NIRD research data archive and available at [https://archive](https://archive.sigma2.no/pages/public/datasetDetail.jsf?id=10.11582/2023.00129)
1068 [.sigma2.no/pages/public/datasetDetail.jsf?id=10.11582/2023.00129](https://archive.sigma2.no/pages/public/datasetDetail.jsf?id=10.11582/2023.00129).

Table 3. CORE-II hydrography bias (root mean square error) reduction compared to the bias of the control case. The observational data sets are the WOA 2018 climatologies for temperature (Locarnini et al., 2018) and salinity (Zweng et al., 2018). The experiment names correspond to parameterizations in Figure 4 as follows: ‘ L_T ’ and ‘ $0.5 \cdot L_T$ ’ correspond to (VIII), with $a_t = 1$ and $a_t = 0.5$, respectively; ‘ L_T and E_{eff} ’ and ‘ $0.5 \cdot L_T$ and E_{eff} ’ correspond to (IX), with $a_t = 1$ and $a_t = 0.5$, respectively. Experiment E_{eff} does not have a counterpart in Figure 4, but uses parameterization like (IX), with the exception that L_T is not considered as a length scale.

Name	zonal mean T	zonal mean S	$T_{100-200m}$	$T_{200-500m}$	$T_{500-1000m}$
Control anom.	0.89°C	0.06 g/kg	1.28°C	1.11°C	0.85°C
L_T	3.3%	2.9%	-1.8%	1.5%	3.4%
$0.5 \cdot L_T$	7.1%	7.0%	-3.8%	3.1%	7.3%
E_{eff}	16%	15%	-11%	4.9%	15%
L_T and E_{eff}	18%	16%	-13%	5.9%	20%
$0.5 \cdot L_T$ and E_{eff}	19%	18%	-15%	5.8%	22%

Table 4. Observed and simulated current transport in selected straits. The various perturbation experiments show percentage changes relative to the control case. The references for the observational values are as follows: Arctic Ocean gateway transports come from de Boer et al. (2018) with the original citations being Ingvaldsen et al. (2004) for Barents Sea Opening, Beszczynska-Möller et al. (2015) for Fram Strait, Curry et al. (2014) for Davis Strait (CAA), and Woodgate (2018); Woodgate et al. (2015) for Bering Strait; ACC transport come from Xu et al. (2020), for pure observational estimates see Koenig et al. (2014) and Donohue et al. (2016); and Florida–Bahamas Strait transport come from Larsen and Sanford (1985)

Name	obs	control	L_T	$0.5 \cdot L_T$	E_{eff}	L_T and E_{eff}	$0.5 \cdot L_T$ and E_{eff}
Barents Opening	2.1 Sv	2.4 Sv	0%	1%	4%	6%	7%
Bering Strait	1.0 Sv	0.7 Sv	2%	3%	5%	7%	8%
Canadian Arctic	-1.7 Sv	-1.6 Sv	4%	8%	14%	15%	16%
Fram Strait	-2.2 Sv	-1.3 Sv	-3%	-6%	-9%	-6%	-6%
Drake Passage (ACC)	157.3 Sv	152 Sv	0%	1%	4%	5%	7%
Florida–Bahamas Strait	32 Sv	13.2 Sv	1%	3%	4%	5%	6%

1069 **Acknowledgments**

1070 We thank the editor, Stephen Griffies, and three anonymous reviewers for their comments
 1071 and suggestions that led to a much improved manuscript. This work was funded in part
 1072 by the two Research Council of Norway projects KeyClim (295046) and TopArctic (314826).
 1073 A. Nummelin would like to thank Mats Bentsen for the help with the initial model setup.

1074 **References**

- 1075 Abernathey, R., & Cessi, P. (2014). Topographic enhancement of eddy efficiency in
 1076 baroclinic equilibrium. *J. Phys. Oceanogr.*, *44*, 2017–2126.
- 1077 Abernathey, R., Ferreira, D., & Klocker, A. (2013). Diagnostics of isopycnal mix-
 1078 ing in a circumpolar channel. *Ocean Modelling*, *72*, 1 - 16. Retrieved from
 1079 <http://www.sciencedirect.com/science/article/pii/S1463500313001200>
 1080 doi: <https://doi.org/10.1016/j.ocemod.2013.07.004>
- 1081 Adcroft, A., Anderson, W., Balaji, V., Blanton, C., Bushuk, M., Dufour, C. O.,
 1082 ... Zhang, R. (2019). The gfdl global ocean and sea ice model om4.0:
 1083 Model description and simulation features. *Journal of Advances in*
 1084 *Modeling Earth Systems*, *11*(10), 3167-3211. Retrieved from [https://](https://agupubs.onlinelibrary.wiley.com/doi/abs/10.1029/2019MS001726)
 1085 agupubs.onlinelibrary.wiley.com/doi/abs/10.1029/2019MS001726 doi:
 1086 <https://doi.org/10.1029/2019MS001726>
- 1087 Bachman, S. D. (2019). The GM+E closure: A framework for coupling backscatter
 1088 with the Gent and McWilliams parameterization. *Ocean Modelling*, *136*, 85 -
 1089 106. Retrieved from [http://www.sciencedirect.com/science/article/pii/](http://www.sciencedirect.com/science/article/pii/S1463500318301975)
 1090 [S1463500318301975](http://www.sciencedirect.com/science/article/pii/S1463500318301975) doi: <https://doi.org/10.1016/j.ocemod.2019.02.006>
- 1091 Bachman, S. D., Fox-Kemper, B., & Bryan, F. O. (2020). A diagnosis of anisotropic
 1092 eddy diffusion from a high-resolution global ocean model. *Journal of Advances*
 1093 *in Modeling Earth Systems*, *12*(2), e2019MS001904. Retrieved from [https://](https://agupubs.onlinelibrary.wiley.com/doi/abs/10.1029/2019MS001904)
 1094 agupubs.onlinelibrary.wiley.com/doi/abs/10.1029/2019MS001904 doi:
 1095 [10.1029/2019MS001904](https://doi.org/10.1029/2019MS001904)
- 1096 Beszczynska-Möller, A., von Appen, W.-J., & Fahrback, E. (2015). *Physical oceanog-*
 1097 *raphy and current meter data from moorings F1-F14 and F15/F16 in the Fram*
 1098 *Strait, 1997-2012* [data set]. PANGAEA. Retrieved from [https://doi.org/](https://doi.org/10.1594/PANGAEA.150016)
 1099 [10.1594/PANGAEA.150016](https://doi.org/10.1594/PANGAEA.150016) doi: [10.1594/PANGAEA.150016](https://doi.org/10.1594/PANGAEA.150016)
- 1100 Blumsack, S. L., & Gierasch, P. J. (1972). Mars: The effects of topography on baro-
 1101 clinic instability. *J. Atmos. Sci.*, *29*, 1081-1089.
- 1102 Bretherton, F. P., & Haidvogel, D. (1976). Two-dimensional turbulence over topogra-
 1103 phy. *J. Fluid. Mech.*, *78*, 129–154.
- 1104 Brink, K. H. (2012). Baroclinic instability of an idealized tidal mixing front. *J. Mar.*
 1105 *Res.*, *70*(4), 661–688.
- 1106 Brink, K. H. (2016). Cross-shelf exchange. *Annual Review of Marine Science*, *8*(1),
 1107 59-78. Retrieved from [https://doi.org/10.1146/annurev-marine-010814-](https://doi.org/10.1146/annurev-marine-010814-015717)
 1108 [-015717](https://doi.org/10.1146/annurev-marine-010814-015717) (PMID: 26747520) doi: [10.1146/annurev-marine-010814-015717](https://doi.org/10.1146/annurev-marine-010814-015717)
- 1109 Buongiorno Nardelli, B. (2020). A multi-year time series of observation-based 3d
 1110 horizontal and vertical quasi-geostrophic global ocean currents. *Earth System*
 1111 *Science Data*, *12*(3), 1711–1723. Retrieved from [https://essd.copernicus](https://essd.copernicus.org/articles/12/1711/2020/)
 1112 [.org/articles/12/1711/2020/](https://essd.copernicus.org/articles/12/1711/2020/) doi: [10.5194/essd-12-1711-2020](https://doi.org/10.5194/essd-12-1711-2020)
- 1113 Busecke, J. J. M., & Abernathey, R. P. (2019). Ocean mesoscale mixing linked to
 1114 climate variability. *Science Advances*, *5*(1). Retrieved from [http://advances](http://advances.sciencemag.org/content/5/1/eaav5014)
 1115 [.sciencemag.org/content/5/1/eaav5014](http://advances.sciencemag.org/content/5/1/eaav5014) doi: [10.1126/sciadv.aav5014](https://doi.org/10.1126/sciadv.aav5014)
- 1116 Chang, P., Zhang, S., Danabasoglu, G., Yeager, S. G., Fu, H., Wang, H., ... Wu,
 1117 L. (2020). An unprecedented set of high-resolution earth system simulations
 1118 for understanding multiscale interactions in climate variability and change.
 1119 *Journal of Advances in Modeling Earth Systems*, *12*(12), e2020MS002298.
 1120 Retrieved from [https://agupubs.onlinelibrary.wiley.com/doi/abs/](https://agupubs.onlinelibrary.wiley.com/doi/abs/10.1029/2020MS002298)
 1121 [10.1029/2020MS002298](https://doi.org/10.1029/2020MS002298) (e2020MS002298 2020MS002298) doi: [https://](https://doi.org/10.1029/2020MS002298)

- doi.org/10.1029/2020MS002298
- 1122
1123 Chen, R., Flierl, G. R., & Wunsch, C. (2014). A description of local and nonlocal
1124 eddy–mean flow interaction in a global eddy-permitting state estimate. *Journal of Physical Oceanography*, *44*(9), 2336 - 2352. Retrieved from <https://journals.ametsoc.org/view/journals/phoc/44/9/jpo-d-14-0009.1.xml>
1125
1126 doi: <https://doi.org/10.1175/JPO-D-14-0009.1>
- 1127
- 1128 Curry, B., Lee, C. M., Petrie, B., Moritz, R. E., & Kwok, R. (2014). Multi-
1129 year volume, liquid freshwater, and sea ice transports through davis strait,
1130 2004–10. *Journal of Physical Oceanography*, *44*(4), 1244 - 1266. Re-
1131 trieved from <https://journals.ametsoc.org/view/journals/phoc/44/4/jpo-d-13-0177.1.xml> doi: 10.1175/JPO-D-13-0177.1
- 1132
- 1133 de Boer, A. M., Gavilan Pascual-Ahuir, E., Stevens, D. P., Chafik, L., Hutchin-
1134 son, D. K., Zhang, Q., ... Willmott, A. J. (2018). Interconnectivity
1135 between volume transports through arctic straits. *Journal of Geophys-
1136 ical Research: Oceans*, *123*(12), 8714-8729. Retrieved from <https://agupubs.onlinelibrary.wiley.com/doi/abs/10.1029/2018JC014320> doi:
1137 <https://doi.org/10.1029/2018JC014320>
- 1138
- 1139 de La Lama, M., Lacasce, J. H., & Fuhr, H. K. (2016). The vertical structure of
1140 ocean eddies. *Dynamics and Statistics of the Climate System*, *1*(1), 1–16. doi:
1141 [10.1093/climsys/dzw001](https://doi.org/10.1093/climsys/dzw001)
- 1142
- 1143 Donohue, K. A., Tracey, K. L., Watts, D. R., Chidichimo, M. P., & Chereskin, T. K.
1144 (2016). Mean antarctic circumpolar current transport measured in drake
1145 passage. *Geophysical Research Letters*, *43*(22), 11,760-11,767. Retrieved
1146 from <https://agupubs.onlinelibrary.wiley.com/doi/abs/10.1002/2016GL070319> doi: <https://doi.org/10.1002/2016GL070319>
- 1147
- 1148 Döös, K., Nycander, J., & Coward, A. C. (2008). Lagrangian decomposition of the
1149 deacon cell. *Journal of Geophysical Research: Oceans*, *113*(C7). Retrieved
1150 from <https://agupubs.onlinelibrary.wiley.com/doi/abs/10.1029/2007JC004351> doi: <https://doi.org/10.1029/2007JC004351>
- 1151
- 1152 Eady, E. T. (1949). Long waves and cyclone waves. *Tellus*, *1*(3), 33-52. Re-
1153 trieved from [https://onlinelibrary.wiley.com/doi/abs/10.1111/](https://onlinelibrary.wiley.com/doi/abs/10.1111/j.2153-3490.1949.tb01265.x)
1154 [j.2153-3490.1949.tb01265.x](https://onlinelibrary.wiley.com/doi/abs/10.1111/j.2153-3490.1949.tb01265.x) doi: 10.1111/j.2153-3490.1949.tb01265.x
- 1155
- 1156 Eden, C. (2007). Eddy length scales in the North Atlantic Ocean. *J. Geophys. Res.*,
1157 *112*(C06004). doi: 10.1029/2006JC003901
- 1158
- 1159 Eden, C., & Greatbatch, R. J. (2008). Towards a mesoscale eddy closure. *Ocean
1160 Modelling*, *20*(3), 223 - 239. Retrieved from [http://www.sciencedirect.com/](http://www.sciencedirect.com/science/article/pii/S1463500307001163)
1161 [science/article/pii/S1463500307001163](http://www.sciencedirect.com/science/article/pii/S1463500307001163) doi: [https://doi.org/10.1016/](https://doi.org/10.1016/j.ocemod.2007.09.002)
1162 [j.ocemod.2007.09.002](https://doi.org/10.1016/j.ocemod.2007.09.002)
- 1163
- 1164 Ferrari, R., & Nikurashin, M. (2010). Suppression of eddy diffusivity across jets in
1165 the southern ocean. *Journal of Physical Oceanography*, *40*(7), 1501-1519. doi:
1166 [10.1175/2010JPO4278.1](https://doi.org/10.1175/2010JPO4278.1)
- 1167
- 1168 Fox-Kemper, B., Adcroft, A., nging, C. W. B., Chassignet, E. P., Curchitser,
1169 E., Danabasoglu, G., ... Yeager, S. G. (2019, feb). Challenges and
1170 prospects in ocean circulation models. *Frontiers in Marine Science*, *6*. doi:
1171 [10.3389/fmars.2019.00065](https://doi.org/10.3389/fmars.2019.00065)
- 1172
- 1173 Fox-Kemper, B., Ferrari, R., & Hallberg, R. (2008). Parameterization of mixed
1174 layer eddies. part i: Theory and diagnosis. *Journal of Physical Oceanography*,
1175 *38*(6), 1145 - 1165. Retrieved from [https://journals.ametsoc.org/view/](https://journals.ametsoc.org/view/journals/phoc/38/6/2007jpo3792.1.xml)
1176 [journals/phoc/38/6/2007jpo3792.1.xml](https://journals.ametsoc.org/view/journals/phoc/38/6/2007jpo3792.1.xml) doi: <https://doi.org/10.1175/2007JPO3792.1>
- 1177
- 1178 Frajka-Williams, E., Anson, I. J., Baehr, J., Bryden, H. L., Chidichimo, M. P.,
1179 Cunningham, S. A., ... Wilson, C. (2019). Atlantic meridional overturning
1180 circulation: Observed transport and variability. *Frontiers in Marine Science*,
1181 *6*. Retrieved from [https://www.frontiersin.org/articles/10.3389/](https://www.frontiersin.org/articles/10.3389/fmars.2019.00260)
1182 [fmars.2019.00260](https://www.frontiersin.org/articles/10.3389/fmars.2019.00260) doi: 10.3389/fmars.2019.00260

- 1177 Fratantoni, D. M. (2001). North Atlantic surface circulation during the 1990's ob-
 1178 served with satellite-tracked drifters. *Journal of Geophysical Research: Oceans*
 1179 (1978–2012), 106(C10), 22067–22093.
- 1180 Gent, P. R. (2011). The gent–mcwilliams parameterization: 20/20 hindsight. *Ocean*
 1181 *Modelling*, 39(1), 2 - 9. Retrieved from [https://doi.org/10.1016/j.ocemod](https://doi.org/10.1016/j.ocemod.2010.08.002)
 1182 .2010.08.002 doi: 0.1016/j.ocemod.2010.08.002
- 1183 Gent, P. R., & McWilliams, J. C. (1990). Isopycnal mixing in ocean circulation
 1184 models. *Journal of Physical Oceanography*, 20(1), 150-155. Retrieved from
 1185 [https://doi.org/10.1175/1520-0485\(1990\)020<0150:IMIOCM>2.0.CO;2](https://doi.org/10.1175/1520-0485(1990)020<0150:IMIOCM>2.0.CO;2)
 1186 doi: 10.1175/1520-0485(1990)020(0150:IMIOCM)2.0.CO;2
- 1187 Gent, P. R., Willebrand, J., McDougall, T. J., & McWilliams, J. C. (1995).
 1188 Parameterizing eddy-induced tracer transports in ocean circulation mod-
 1189 els. *Journal of Physical Oceanography*, 25(4), 463-474. Retrieved from
 1190 [https://doi.org/10.1175/1520-0485\(1995\)025<0463:PEITTI>2.0.CO;2](https://doi.org/10.1175/1520-0485(1995)025<0463:PEITTI>2.0.CO;2)
 1191 doi: 10.1175/1520-0485(1995)025(0463:PEITTI)2.0.CO;2
- 1192 Green, J. S. (1970). Transfer properties of the large-scale eddies and the general cir-
 1193 culation of the atmosphere. *Quart. J. Roy. Meteor. Soc.*, 96, 157–185.
- 1194 Haidvogel, D. B., & Brink, K. H. (1986). Mean currents driven by topographic drag
 1195 over the continental shelf and slope. *J. Phys. Oceanogr.*, 16, 2159–2171.
- 1196 Hallberg, R. (2013). Using a resolution function to regulate parameterizations of
 1197 oceanic mesoscale eddy effects. *Ocean Modelling*, 72, 92 - 103. Retrieved from
 1198 <https://doi.org/10.1016/j.ocemod.2013.08.007> doi: 10.1016/j.ocemod
 1199 .2013.08.007
- 1200 Held, I. M., & Larichev, V. D. (1996). A scaling theory for horizontally homo-
 1201 geneous, baroclinically unstable flow on a beta plane. *Journal of the At-*
 1202 *mospheric Sciences*, 53(7), 946-952. Retrieved from [https://doi.org/](https://doi.org/10.1175/1520-0469(1996)053<0946:ASTFHH>2.0.CO;2)
 1203 [10.1175/1520-0469\(1996\)053<0946:ASTFHH>2.0.CO;2](https://doi.org/10.1175/1520-0469(1996)053<0946:ASTFHH>2.0.CO;2) doi: 10.1175/
 1204 1520-0469(1996)053(0946:ASTFHH)2.0.CO;2
- 1205 Hetland, R. D. (2017). Suppression of baroclinic instabilities in buoyancy-driven flow
 1206 over sloping bathymetry. *J. Phys. Oceanogr.*, 47(1). doi: 10.1175/JPO-D-15
 1207 -0240.1
- 1208 Holmes, R. M., Groeskamp, S., Stewart, K. D., & McDougall, T. J. (2022). Sensi-
 1209 tivity of a coarse-resolution global ocean model to a spatially variable neu-
 1210 tral diffusivity. *Journal of Advances in Modeling Earth Systems*, 14(3),
 1211 e2021MS002914. Retrieved from [https://agupubs.onlinelibrary.wiley](https://agupubs.onlinelibrary.wiley.com/doi/abs/10.1029/2021MS002914)
 1212 [.com/doi/abs/10.1029/2021MS002914](https://doi.org/10.1029/2021MS002914) (e2021MS002914 2021MS002914) doi:
 1213 <https://doi.org/10.1029/2021MS002914>
- 1214 Huneke, W. G. C., Klocker, A., & Galton-Fenzi, B. K. (2019). Deep bottom
 1215 mixed layer drives intrinsic variability of the antarctic slope front. *Journal*
 1216 *of Physical Oceanography*, 49(12), 3163 - 3177. Retrieved from [https://](https://journals.ametsoc.org/view/journals/phoc/49/12/jpo-d-19-0044.1.xml)
 1217 journals.ametsoc.org/view/journals/phoc/49/12/jpo-d-19-0044.1.xml
 1218 doi: <https://doi.org/10.1175/JPO-D-19-0044.1>
- 1219 Ingvaldsen, R. B., Asplin, L., & Loeng, H. (2004). Velocity field of the western en-
 1220 trance to the barents sea. *Journal of Geophysical Research: Oceans*, 109(C3).
 1221 Retrieved from [https://agupubs.onlinelibrary.wiley.com/doi/abs/](https://agupubs.onlinelibrary.wiley.com/doi/abs/10.1029/2003JC001811)
 1222 [10.1029/2003JC001811](https://doi.org/10.1029/2003JC001811) doi: <https://doi.org/10.1029/2003JC001811>
- 1223 Isachsen, P. E. (2011). Baroclinic instability and eddy tracer transport across
 1224 sloping bottom topography: How well does a modified eady model do in
 1225 primitive equation simulations? *Ocean Modelling*, 39(1), 183-199. Re-
 1226 trieved from [https://www.sciencedirect.com/science/article/pii/](https://www.sciencedirect.com/science/article/pii/S1463500310001460)
 1227 [S1463500310001460](https://doi.org/10.1016/j.ocemod.2010.09.007) (Modelling and Understanding the Ocean Mesoscale and
 1228 Submesoscale) doi: <https://doi.org/10.1016/j.ocemod.2010.09.007>
- 1229 Jansen, M. F., Adcroft, A., Khani, S., & Kong, H. (2019). Toward an Energeti-
 1230 cally Consistent, Resolution Aware Parameterization of Ocean Mesoscale
 1231 Eddies. *Journal of Advances in Modeling Earth Systems*, 0(0). Retrieved

- 1232 from <https://agupubs.onlinelibrary.wiley.com/doi/abs/10.1029/>
 1233 2019MS001750 doi: 10.1029/2019MS001750
- 1234 Jansen, M. F., Adcroft, A. J., Hallberg, R., & Held, I. M. (2015). Parameterization
 1235 of eddy fluxes based on a mesoscale energy budget. *Ocean Mod.*, *92*, 28–41.
- 1236 Khani, S., Jansen, M. F., & Adcroft, A. (2019). Diagnosing subgrid mesoscale eddy
 1237 fluxes with and without topography. *J. Adv. Mod. Earth Sci.*, *11*, 3995–4015.
 1238 doi: 10.1029/2019MS001721
- 1239 Killworth, P. D. (1992). An equivalent-barotropic mode in the Fine Resolu-
 1240 tion Antarctic Model. *J. Phys. Oceanogr.*, *22*, 1379–1387. doi: 10.1175/
 1241 1520-0485(1992)022
- 1242 Kjellsson, J., & Zanna, L. (2017). The impact of horizontal resolution on energy
 1243 transfers in global ocean models. *Fluids*, *2*(3). Retrieved from [https://www](https://www.mdpi.com/2311-5521/2/3/45)
 1244 [.mdpi.com/2311-5521/2/3/45](https://www.mdpi.com/2311-5521/2/3/45) doi: 10.3390/fluids2030045
- 1245 Klocker, A., Ferrari, R., & LaCasce, J. H. (2012). Estimating suppression of eddy
 1246 mixing by mean flows. *Journal of Physical Oceanography*, *42*(9), 1566–1576.
- 1247 Koenig, Z., Provost, C., Ferrari, R., Sennéchaël, N., & Rio, M.-H. (2014). Volume
 1248 transport of the antarctic circumpolar current: Production and validation of
 1249 a 20 year long time series obtained from in situ and satellite observations.
 1250 *Journal of Geophysical Research: Oceans*, *119*(8), 5407–5433. Retrieved
 1251 from <https://agupubs.onlinelibrary.wiley.com/doi/abs/10.1002/>
 1252 2014JC009966 doi: <https://doi.org/10.1002/2014JC009966>
- 1253 Kong, H., & Jansen, M. F. (2021). The impact of topography and eddy param-
 1254 eterization on the simulated southern ocean circulation response to changes
 1255 in surface wind stress. *Journal of Physical Oceanography*, *51*(3), 825 - 843.
 1256 Retrieved from [https://journals.ametsoc.org/view/journals/phoc/51/3/](https://journals.ametsoc.org/view/journals/phoc/51/3/JPO-D-20-0142.1.xml)
 1257 [JPO-D-20-0142.1.xml](https://journals.ametsoc.org/view/journals/phoc/51/3/JPO-D-20-0142.1.xml) doi: <https://doi.org/10.1175/JPO-D-20-0142.1>
- 1258 Koszalka, I., LaCasce, J., Andersson, M., Orvik, K., & Mauritzen, C. (2011). Sur-
 1259 face circulation in the Nordic Seas from clustered drifters. *Deep-Sea Res. I*,
 1260 *58*, 468–485.
- 1261 LaCasce, J. H. (2000). Floats and f/H. *J. Mar. Res.*, *58*, 61–95.
- 1262 Lacasce, J. H. (2017). The Prevalence of oceanic surface modes. *Geophys. Res.*
 1263 *Lettr.*, *44*(21), 11097–11105. doi: 10.1002/2017GL075430
- 1264 Lacasce, J. H., & Brink, K. (2000). Geostrophic turbulence over a slope. *J. Phys.*
 1265 *Oceanogr.*, *30*, 1305–1324.
- 1266 Larichev, V. D., & Held, I. M. (1995). Eddy amplitudes and fluxes in a homo-
 1267 geneous model of fully developed baroclinic instability. *J. Phys. Oceanogr.*,
 1268 *25*(10), 2285–2297.
- 1269 Larsen, J. C., & Sanford, T. B. (1985). Florida current volume transports from volt-
 1270 age measurements. *Science*, *227*(4684), 302-304. Retrieved from [https://](https://www.science.org/doi/abs/10.1126/science.227.4684.302)
 1271 www.science.org/doi/abs/10.1126/science.227.4684.302 doi: 10.1126/
 1272 [science.227.4684.302](https://www.science.org/doi/abs/10.1126/science.227.4684.302)
- 1273 Liu, M., Chen, R., Guan, W., Zhang, H., & Jing, T. (2023). Nonlocality of scale-
 1274 dependent eddy mixing at the kuroshio extension. *Frontiers in Marine*
 1275 *Science*, *10*. Retrieved from [https://www.frontiersin.org/articles/](https://www.frontiersin.org/articles/10.3389/fmars.2023.1137216)
 1276 [10.3389/fmars.2023.1137216](https://www.frontiersin.org/articles/10.3389/fmars.2023.1137216) doi: 10.3389/fmars.2023.1137216
- 1277 Locarnini, R. A., Mishonov, A. V., Baranova, O. K., Boyer, T. P., Zweng, M. M.,
 1278 Garcia, H. E., ... Smolyar, I. (2018). *World ocean atlas 2018, volume 1:*
 1279 *Temperature. a. mishonov technical ed.* NOAA Atlas NESDIS 81, 52pp. Re-
 1280 trieved from [https://www.ncei.noaa.gov/sites/default/files/2022-06/](https://www.ncei.noaa.gov/sites/default/files/2022-06/woa18_vol11.pdf)
 1281 [woa18_vol11.pdf](https://www.ncei.noaa.gov/sites/default/files/2022-06/woa18_vol11.pdf)
- 1282 Lumpkin, R., & Speer, K. (2007). Global ocean meridional overturning. *Journal*
 1283 *of Physical Oceanography*, *37*(10), 2550 - 2562. Retrieved from [https://](https://journals.ametsoc.org/view/journals/phoc/37/10/jpo3130.1.xml)
 1284 journals.ametsoc.org/view/journals/phoc/37/10/jpo3130.1.xml doi:
 1285 <https://doi.org/10.1175/JPO3130.1>
- 1286 Mak, J., Maddison, J. R., Marshall, D. P., & Munday, D. R. (2018). Implementation

- 1287 of a geometrically informed and energetically constrained mesoscale eddy pa-
 1288 rameterization in an ocean circulation model. *Journal of Physical Oceanogra-*
 1289 *phy*, 0(0), null. Retrieved from <https://doi.org/10.1175/JPO-D-18-0017.1>
 1290 doi: 10.1175/JPO-D-18-0017.1
- 1291 Manucharyan, G. E., & Isachsen, P. E. (2019). Critical Role of Continental Slopes
 1292 in Halocline and Eddy Dynamics of the Ekman-Driven Beaufort Gyre. *J. Geo-*
 1293 *phys. Res.*, 124, 2679–2696. doi: 10.1029/2018JC014624
- 1294 Manucharyan, G. E., & Stewart, A. L. (2022). Stirring of interior potential porticity
 1295 gradients as a formation mechanism for large subsurface-intensified eddies in
 1296 the Beaufort Gyre. *J. Phys. Oceanogr.*, 52, 3349–3370.
- 1297 Marshall, D. P., Maddison, J. R., & Berloff, P. S. (2012). A framework for pa-
 1298 rameterizing eddy potential vorticity fluxes. *Journal of Physical Oceanography*,
 1299 42(4), 539–557. Retrieved from <https://doi.org/10.1175/JPO-D-11-048.1>
 1300 doi: 10.1175/JPO-D-11-048.1
- 1301 Mechoso, C. R. (1980). Baroclinic instability of flows along sloping boundaries. *J.*
 1302 *Atmos. Sci.*, 37, 1393–1399.
- 1303 Meneghello, G., Marshall, J., Lique, C., Isachsen, P. E., Doddridge, E., Campin,
 1304 J.-M., ... Talandier, C. (2021). Genesis and decay of mesoscale baro-
 1305 clinic eddies in the seasonally ice-covered interior arctic ocean. *Journal*
 1306 *of Physical Oceanography*, 51(1), 115 - 129. Retrieved from [https://](https://journals.ametsoc.org/view/journals/phoc/51/1/jpo-d-20-0054.1.xml)
 1307 journals.ametsoc.org/view/journals/phoc/51/1/jpo-d-20-0054.1.xml
 1308 doi: 10.1175/JPO-D-20-0054.1
- 1309 Nummelin, A. (2023a). *Parameterizing mesoscale eddy buoyancy transport over slop-*
 1310 *ing topography – data*. [Dataset]. NIRD research data archive. Retrieved from
 1311 dx.doi.org/10.11582/2023.00129 doi: 10.11582/2023.00129
- 1312 Nummelin, A. (2023b). *Parameterizing mesoscale eddy buoyancy transport over slop-*
 1313 *ing topography – model setup*. [Software]. Zenodo. Retrieved from [dx.doi.org/](https://dx.doi.org/10.5281/zenodo.8227382)
 1314 [10.5281/zenodo.8227382](https://dx.doi.org/10.5281/zenodo.8227382) doi: 10.5281/zenodo.8227382
- 1315 Nummelin, A., Busecke, J. J. M., Haine, T. W. N., & Abernathy, R. P. (2021).
 1316 Diagnosing the scale- and space-dependent horizontal eddy diffusivity at the
 1317 global surface ocean. *Journal of Physical Oceanography*, 51(2), 279 - 297. Re-
 1318 trieved from [https://journals.ametsoc.org/view/journals/phoc/51/2/](https://journals.ametsoc.org/view/journals/phoc/51/2/jpo-d-19-0256.1.xml)
 1319 [jpo-d-19-0256.1.xml](https://journals.ametsoc.org/view/journals/phoc/51/2/jpo-d-19-0256.1.xml) doi: 10.1175/JPO-D-19-0256.1
- 1320 Nøst, O. A., & Isachsen, P. E. (2003). The large-scale time-mean ocean circulation
 1321 in the Nordic Seas and Arctic Ocean estimated from simplified dynamics. *J.*
 1322 *Mar. Res.*, 61, 175–210.
- 1323 Ong, E. Q. Y., Doddridge, E., Constantinou, N. C., Hogg, A. M., & England, M. H.
 1324 (2023). *Intrinsically episodic antarctic shelf intrusions of circumpolar deep*
 1325 *water via canyons*. doi: 10.48550/arXiv.2304.13225
- 1326 Prandtl, L. (1925). 7. Bericht über Untersuchungen zur ausgebildeten Turbu-
 1327 lenz. *Zeitschrift Angewandte Mathematik und Mechanik*, 5(2), 136–139. doi:
 1328 10.1002/zamm.19250050212
- 1329 Redi, M. H. (1982). Oceanic isopycnal mixing by coordinate rotation. *Jour-*
 1330 *nal of Physical Oceanography*, 12(10), 1154–1158. Retrieved from [https://doi](https://doi.org/10.1175/1520-0485(1982)012<1154:OIMBCR>2.0.CO;2)
 1331 [.org/10.1175/1520-0485\(1982\)012<1154:OIMBCR>2.0.CO;2](https://doi.org/10.1175/1520-0485(1982)012<1154:OIMBCR>2.0.CO;2) doi: 10.1175/
 1332 1520-0485(1982)012<1154:OIMBCR>2.0.CO;2
- 1333 Rhines, P. (1977). The dynamics of unsteady currents. In *The sea* (Vol. 6,
 1334 p. 189–318). New York: Wiley.
- 1335 Sandwell, D. T., Goff, J. A., Gevorgian, J., Harper, H., Kim, S.-S., Yu, Y., ...
 1336 Smith, W. H. F. (2022). Improved bathymetric prediction using geologi-
 1337 cal information: Synbath. *Earth and Space Science*, 9(2), e2021EA002069.
 1338 Retrieved from [https://agupubs.onlinelibrary.wiley.com/doi/abs/](https://agupubs.onlinelibrary.wiley.com/doi/abs/10.1029/2021EA002069)
 1339 [10.1029/2021EA002069](https://agupubs.onlinelibrary.wiley.com/doi/abs/10.1029/2021EA002069) (e2021EA002069 2021EA002069) doi: [https://](https://doi.org/10.1029/2021EA002069)
 1340 doi.org/10.1029/2021EA002069
- 1341 Seland, Ø., Bentsen, M., Olivié, D., Toniazzo, T., Gjermundsen, A., Graff, L. S.,

- 1342 ... Schulz, M. (2020). Overview of the norwegian earth system model
 1343 (noesm2) and key climate response of cmip6 deck, historical, and scenario
 1344 simulations. *Geoscientific Model Development*, *13*(12), 6165–6200. Re-
 1345 trieved from <https://gmd.copernicus.org/articles/13/6165/2020/> doi:
 1346 10.5194/gmd-13-6165-2020
- 1347 Smith, K. S., & Marshall, J. (2009). Evidence for Enhanced Eddy Mixing at Mid-
 1348 depth in the Southern Ocean. *Journal of Physical Oceanography*, *39*(1),
 1349 50-69. Retrieved from <https://doi.org/10.1175/2008JP03880.1> doi:
 1350 10.1175/2008JPO3880.1
- 1351 Smith, R. D., & Gent, P. R. (2004). Anisotropic gent-mcwilliams parameteriza-
 1352 tion for ocean models. *Journal of Physical Oceanography*, *34*(11), 2541-2564.
 1353 Retrieved from <https://doi.org/10.1175/JPO2613.1> doi: 10.1175/JPO2613
 1354 .1
- 1355 Speer, K., Rintoul, S. R., & Sloyan, B. (2000). The diabatic deacon cell.
 1356 *Journal of Physical Oceanography*, *30*(12), 3212 - 3222. Retrieved from
 1357 [https://journals.ametsoc.org/view/journals/phoc/30/12/1520](https://journals.ametsoc.org/view/journals/phoc/30/12/1520-0485_2000_030_3212_tddc_2.0.co_2.xml)
 1358 [-0485_2000_030_3212_tddc_2.0.co_2.xml](https://journals.ametsoc.org/view/journals/phoc/30/12/1520-0485_2000_030_3212_tddc_2.0.co_2.xml) doi: [https://doi.org/10.1175/](https://doi.org/10.1175/1520-0485(2000)030(3212:TDDC)2.0.CO;2)
 1359 [1520-0485\(2000\)030\(3212:TDDC\)2.0.CO;2](https://doi.org/10.1175/1520-0485(2000)030(3212:TDDC)2.0.CO;2)
- 1360 Stammer, D. (1997). Global Characteristics of Ocean Variability Estimated from Re-
 1361 gional TOPEX/POSEIDON Altimeter Measurements. *J. Phys. Oceanogr.*, *27*,
 1362 1743–1769.
- 1363 Stanley, Z., Bachman, S. D., & Grooms, I. (2020). Vertical structure of ocean
 1364 mesoscale eddies with implications for parameterizations of tracer transport.
 1365 *Journal of Advances in Modeling Earth Systems*, *12*(10), e2020MS002151.
 1366 Retrieved from [https://agupubs.onlinelibrary.wiley.com/doi/abs/](https://agupubs.onlinelibrary.wiley.com/doi/abs/10.1029/2020MS002151)
 1367 [10.1029/2020MS002151](https://doi.org/10.1029/2020MS002151) doi: <https://doi.org/10.1029/2020MS002151>
- 1368 Stewart, A. L., Neumann, N. K., & Solodoch, A. (2023). "Eddy" saturation of the
 1369 Antarctic Circumpolar Current by standing waves. *J. Phys. Oceanogr.* doi: 10
 1370 .1175/JPO-D-22-0154.1
- 1371 Stewart, K., Spence, P., Waterman, S., Sommer, J. L., Molines, J.-M., Lilly, J., &
 1372 England, M. (2015). Anisotropy of eddy variability in the global ocean. *Ocean*
 1373 *Modelling*, *95*, 53-65. Retrieved from [https://www.sciencedirect.com/](https://www.sciencedirect.com/science/article/pii/S1463500315001638)
 1374 [science/article/pii/S1463500315001638](https://www.sciencedirect.com/science/article/pii/S1463500315001638) doi: [https://doi.org/10.1016/](https://doi.org/10.1016/j.ocemod.2015.09.005)
 1375 [j.ocemod.2015.09.005](https://doi.org/10.1016/j.ocemod.2015.09.005)
- 1376 Stone, P. (1972). A simplified radiative-dynamical model for the static stability of
 1377 rotating atmospheres. *J. Atmos. Sci.*, *29*, 405-418.
- 1378 Sutyrin, G. G., Radko, T., & Nycander, J. (2021). Steady radiating baroclinic vor-
 1379 tices in vertically sheared flows. *Physics of Fluids*, *33*(3), 031705. Retrieved
 1380 from <https://doi.org/10.1063/5.0040298> doi: 10.1063/5.0040298
- 1381 Trenberth, K. E., Zhang, Y., Fasullo, J. T., & Cheng, L. (2019). Observa-
 1382 tion-based estimates of global and basin ocean meridional heat transport time
 1383 series. *Journal of Climate*, *32*(14), 4567 - 4583. Retrieved from [https://](https://journals.ametsoc.org/view/journals/clim/32/14/jcli-d-18-0872.1.xml)
 1384 journals.ametsoc.org/view/journals/clim/32/14/jcli-d-18-0872.1.xml
 1385 doi: <https://doi.org/10.1175/JCLI-D-18-0872.1>
- 1386 Trodahl, M., & Isachsen, P. E. (2018). Topographic influence on baroclinic insta-
 1387 bility and the mesoscale eddy field in the northern north atlantic ocean and
 1388 the nordic seas. *Journal of Physical Oceanography*, *48*(11), 2593 - 2607. Re-
 1389 trieved from [https://journals.ametsoc.org/view/journals/phoc/48/11/](https://journals.ametsoc.org/view/journals/phoc/48/11/jpo-d-17-0220.1.xml)
 1390 [jpo-d-17-0220.1.xml](https://journals.ametsoc.org/view/journals/phoc/48/11/jpo-d-17-0220.1.xml) doi: 10.1175/JPO-D-17-0220.1
- 1391 Tsujino, H., Urakawa, L. S., Griffies, S. M., Danabasoglu, G., Adcroft, A. J., Ama-
 1392 ral, A. E., ... Yu, Z. (2020). Evaluation of global ocean-sea-ice model simula-
 1393 tions based on the experimental protocols of the ocean model intercomparison
 1394 project phase 2 (omip-2). *Geoscientific Model Development*, *13*(8), 3643–3708.
 1395 Retrieved from <https://gmd.copernicus.org/articles/13/3643/2020/>
 1396 doi: 10.5194/gmd-13-3643-2020

- 1397 Uchida, T., Jamet, Q., Dewar, W. K., Le Sommer, J., Penduff, T., & Balwada, D.
1398 (2022). Diagnosing the thickness-weighted averaged eddy-mean flow interaction
1399 from an eddying north atlantic ensemble: The eliasen-palm flux. *Journal*
1400 *of Advances in Modeling Earth Systems*, *14*(5), e2021MS002866. Retrieved
1401 from [https://agupubs.onlinelibrary.wiley.com/doi/abs/10.1029/](https://agupubs.onlinelibrary.wiley.com/doi/abs/10.1029/2021MS002866)
1402 [2021MS002866](https://doi.org/10.1029/2021MS002866) (e2021MS002866 2021MS002866) doi: [https://doi.org/10.1029/](https://doi.org/10.1029/2021MS002866)
1403 [2021MS002866](https://doi.org/10.1029/2021MS002866)
- 1404 Vallis, G., & Maltrud, M. E. (1993). Generation of mean flows and jets on a beta-
1405 plane and over topography. *J. Phys. Oceanogr.*, *23*, 1346-1362.
- 1406 Visbeck, M., Marshall, J., Haine, T., & Spall, M. (1997). Specification of eddy transfer
1407 coefficients in coarse-resolution ocean circulation models. *Journal of Physical*
1408 *Oceanography*, *27*(3), 381-402. Retrieved from [https://doi.org/10.1175/](https://doi.org/10.1175/1520-0485(1997)027<0381:SOETCI>2.0.CO;2)
1409 [1520-0485\(1997\)027<0381:SOETCI>2.0.CO;2](https://doi.org/10.1175/1520-0485(1997)027(0381:SOETCI)2.0.CO;2) doi: [10.1175/1520-0485\(1997\)](https://doi.org/10.1175/1520-0485(1997)027(0381:SOETCI)2.0.CO;2)
1410 [027\(0381:SOETCI\)2.0.CO;2](https://doi.org/10.1175/1520-0485(1997)027(0381:SOETCI)2.0.CO;2)
- 1411 Wang, Y., & Stewart, A. L. (2018). Eddy dynamics over continental slopes
1412 under retrograde winds: Insights from a model inter-comparison. *Ocean*
1413 *Modelling*, *121*, 1-18. Retrieved from [https://www.sciencedirect.com/](https://www.sciencedirect.com/science/article/pii/S146350031730183X)
1414 [science/article/pii/S146350031730183X](https://www.sciencedirect.com/science/article/pii/S146350031730183X) doi: [https://doi.org/10.1016/](https://doi.org/10.1016/j.ocemod.2017.11.006)
1415 [j.ocemod.2017.11.006](https://doi.org/10.1016/j.ocemod.2017.11.006)
- 1416 Wang, Y., & Stewart, A. L. (2020). Scalings for eddy buoyancy transfer across
1417 continental slopes under retrograde winds. *Ocean Modelling*, *147*, 101579.
1418 Retrieved from [https://www.sciencedirect.com/science/article/pii/](https://www.sciencedirect.com/science/article/pii/S1463500319301775)
1419 [S1463500319301775](https://www.sciencedirect.com/science/article/pii/S1463500319301775) doi: <https://doi.org/10.1016/j.ocemod.2020.101579>
- 1420 Wei, H., & Wang, Y. (2021). Full-depth scalings for isopycnal eddy mixing across
1421 continental slopes under upwelling-favorable winds. *Journal of Advances in*
1422 *Modeling Earth Systems*, *13*(6), e2021MS002498. Retrieved from [https://](https://agupubs.onlinelibrary.wiley.com/doi/abs/10.1029/2021MS002498)
1423 agupubs.onlinelibrary.wiley.com/doi/abs/10.1029/2021MS002498 doi:
1424 <https://doi.org/10.1029/2021MS002498>
- 1425 Wei, H., Wang, Y., Stewart, A. L., & Mak, J. (2022). Scalings for eddy
1426 buoyancy fluxes across prograde shelf/slope fronts. *Journal of Ad-*
1427 *vances in Modeling Earth Systems*, *14*(12), e2022MS003229. Retrieved
1428 from [https://agupubs.onlinelibrary.wiley.com/doi/abs/10.1029/](https://agupubs.onlinelibrary.wiley.com/doi/abs/10.1029/2022MS003229)
1429 [2022MS003229](https://agupubs.onlinelibrary.wiley.com/doi/abs/10.1029/2022MS003229) (e2022MS003229 2022MS003229) doi: [https://doi.org/10.1029/](https://doi.org/10.1029/2022MS003229)
1430 [2022MS003229](https://doi.org/10.1029/2022MS003229)
- 1431 Woodgate, R. A. (2018). Increases in the pacific inflow to the arctic from 1990 to
1432 2015, and insights into seasonal trends and driving mechanisms from year-
1433 round bering strait mooring data. *Progress in Oceanography*, *160*, 124-154.
1434 Retrieved from [https://www.sciencedirect.com/science/article/pii/](https://www.sciencedirect.com/science/article/pii/S0079661117302215)
1435 [S0079661117302215](https://www.sciencedirect.com/science/article/pii/S0079661117302215) doi: <https://doi.org/10.1016/j.pocean.2017.12.007>
- 1436 Woodgate, R. A., Stafford, K. M., & Prah, F. G. (2015). A synthesis of
1437 year-round interdisciplinary mooring measurements in the bering strait
1438 (1990–2014) and the rusalca years (2004–2011). *Oceanography*. Retrieved
1439 from <https://doi.org/10.5670/oceanog.2015.57>
- 1440 Wunsch, C. (1997). The vertical partition of oceanic horizontal kinetic energy. *J.*
1441 *Phys. Oceanogr.*, *27*, 1770–1794.
- 1442 Xu, X., Chassignet, E. P., Firing, Y. L., & Donohue, K. (2020). Antarctic cir-
1443 cumpolar current transport through drake passage: What can we learn from
1444 comparing high-resolution model results to observations? *Journal of Geophys-*
1445 *ical Research: Oceans*, *125*(7), e2020JC016365. Retrieved from [https://](https://agupubs.onlinelibrary.wiley.com/doi/abs/10.1029/2020JC016365)
1446 agupubs.onlinelibrary.wiley.com/doi/abs/10.1029/2020JC016365
1447 [\(e2020JC016365 2020JC016365\) doi: https://doi.org/10.1029/2020JC016365](https://doi.org/10.1029/2020JC016365)
- 1448 Yankovsky, E., Zanna, L., & Smith, K. S. (2022). Influences of mesoscale ocean ed-
1449 dies on flow vertical structure in a resolution-based model hierarchy. *Journal of*
1450 *Advances in Modeling Earth Systems*, *14*(11), e2022MS003203. Retrieved
1451 from <https://agupubs.onlinelibrary.wiley.com/doi/abs/10.1029/>

- 1452 2022MS003203 (e2022MS003203 2022MS003203) doi: [https://doi.org/10.1029/](https://doi.org/10.1029/2022MS003203)
1453 2022MS003203
- 1454 Zhang, G., Chen, R., Li, L., Wei, H., & Sun, S. (2023). Global trends in sur-
1455 face eddy mixing from satellite altimetry. *Frontiers in Marine Science*,
1456 10. Retrieved from [https://www.frontiersin.org/articles/10.3389/](https://www.frontiersin.org/articles/10.3389/fmars.2023.1157049)
1457 [fmars.2023.1157049](https://www.frontiersin.org/articles/10.3389/fmars.2023.1157049) doi: 10.3389/fmars.2023.1157049
- 1458 Zhang, W., & Wolfe, C. L. P. (2022). On the vertical structure of oceanic mesoscale
1459 tracer diffusivities. *Journal of Advances in Modeling Earth Systems*, 14(6),
1460 e2021MS002891. Retrieved from [https://agupubs.onlinelibrary.wiley](https://agupubs.onlinelibrary.wiley.com/doi/abs/10.1029/2021MS002891)
1461 [.com/doi/abs/10.1029/2021MS002891](https://agupubs.onlinelibrary.wiley.com/doi/abs/10.1029/2021MS002891) (e2021MS002891 2021MS002891) doi:
1462 <https://doi.org/10.1029/2021MS002891>
- 1463 Zweng, M. M., Reagan, J. R., Seidov, D., Boyer, T. P., Locarnini, R. A., Gar-
1464 cia, H. E., . . . Smolyar, I. (2018). *World ocean atlas 2018, volume 2:*
1465 *Salinity. a. mishonov technical ed.* NOAA Atlas NESDIS 82, 50pp. Re-
1466 trieved from [https://www.ncei.noaa.gov/sites/default/files/2022-06/](https://www.ncei.noaa.gov/sites/default/files/2022-06/woa18_vol12.pdf)
1467 [woa18_vol12.pdf](https://www.ncei.noaa.gov/sites/default/files/2022-06/woa18_vol12.pdf)

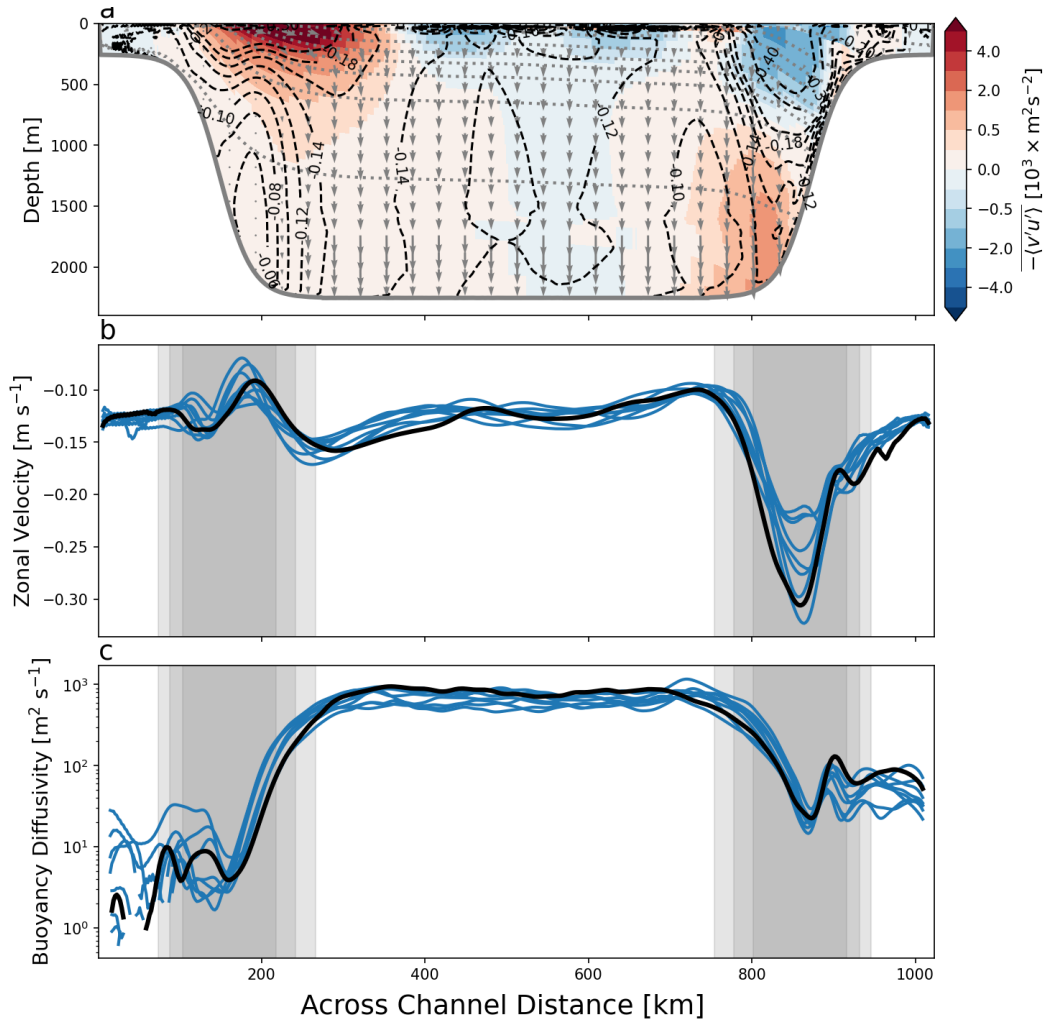


Figure 1. Cross section of zonally and temporally-averaged (a) mean zonal velocity (dashed black contours), mean density (dotted gray contours), E-P flux (gray arrows) and its horizontal component (meridional eddy flux of negative u -momentum; shading, note that the units have been scaled by 10^3 and here the bar denotes time-mean), (b) vertically-averaged zonal velocity and (c) vertically-averaged meridional buoyancy (temperature) diffusivity. In panels b and c the blue lines show results from the various experiments listed in Table 2. The black line is experiment 3 and corresponds to the case shown in panel a. Gray shading shows the location of the slope regions in the different simulations (where $300 \text{ m} < H < 2250 \text{ m}$). For some of the simulations the diffusivity lines are broken because of negative diffusivities that are not shown on the log scale.

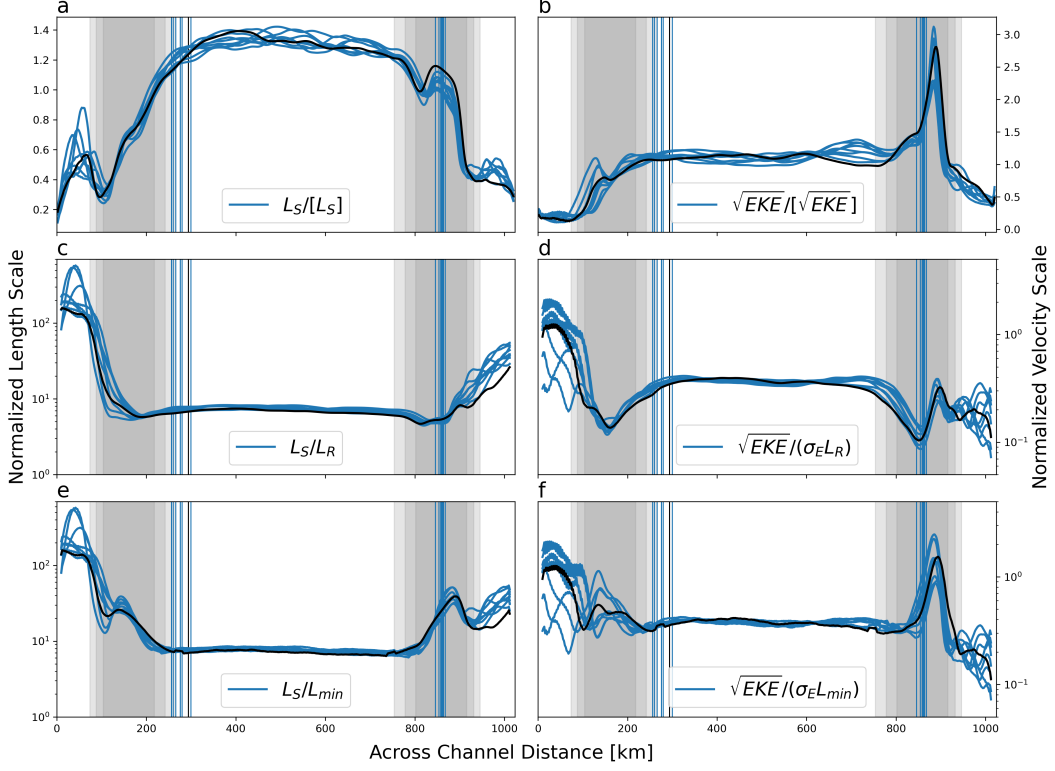


Figure 2. Diagnosed length scales (panels on the left) and velocity scales (panels on the right) for all experiments. All measures are zonal and time averages that have been normalized. The top row (panels a and b) are normalized by the basin-mean values (denoted by square brackets). Length scales in panel c and panel e are normalized by the deformation radius (L_R) and by the minimum of deformation radius and topographic Rhines scale (L_{min}), respectively. In panels d and f we normalize by the parameterized velocity scale, using length scales from c and e, respectively. Colors and line styles as in Fig. 1. Gray shadings indicate the slope regions (similar to Fig. 1) and vertical lines indicate the location of maxima in depth-averaged velocity in each experiment.

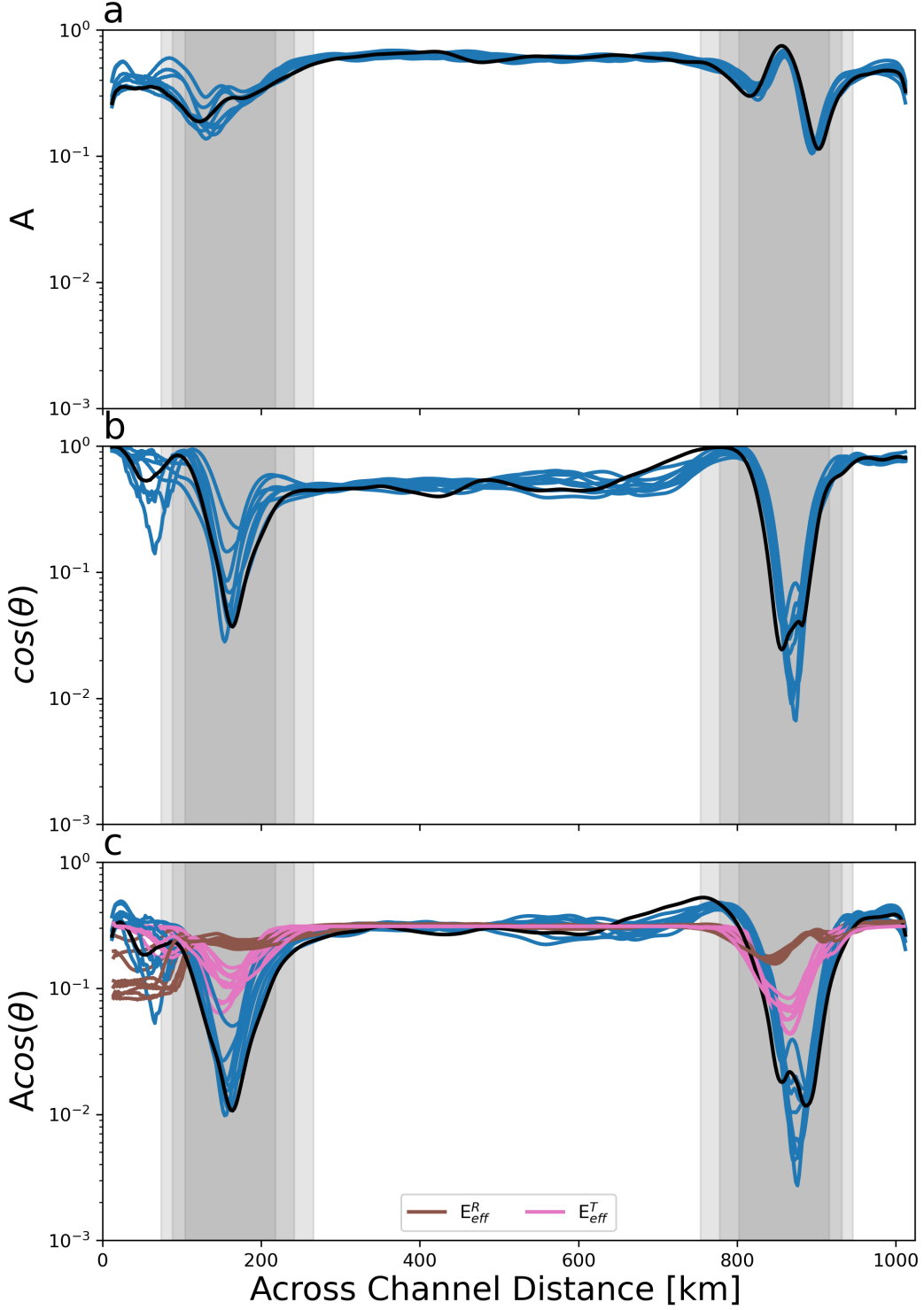


Figure 3. Measures of anisotropy and phase angle relationships: (a) eddy velocity anisotropy (A), (b) cosine of the phase angle between \overline{T}' and \overline{v}' and (c) the product of (a) and (b), as well as the parameterized eddy efficiency factors E_{eff} (brown when using deformation radius, pink when using the topographic Rhines scale). In panel c we use $a_2 = 10$ for E_{eff} . To match the mid-basin values of E_{eff} with $A \cos(\theta)$, we scale E_{eff}^R with 0.35 and E_{eff}^T with 0.32. Colors and line styles as in Fig. 1, and gray shadings indicate the slope regions.

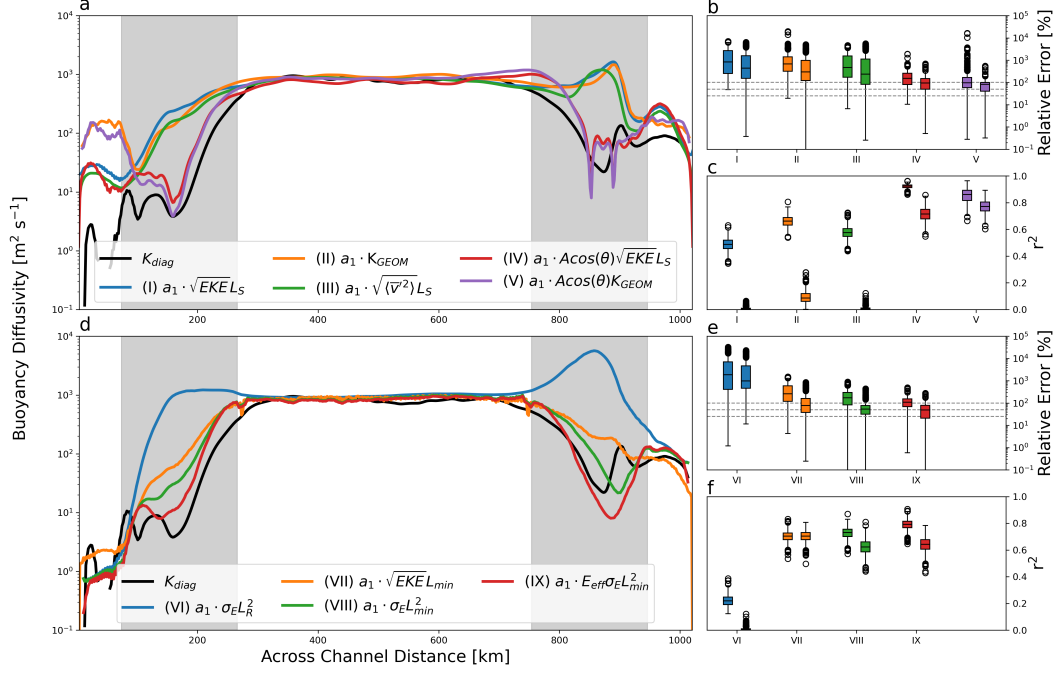


Figure 4. Partly-parameterized (a–c) and fully-parameterized (d–f) across-slope buoyancy diffusivities. The left panels show across-basin profiles for experiment 3 (Table 2) whereas the right panels summarize the statistical comparison between the diagnosed and parameterized diffusivities across all experiments (b–c, e–f; relative error is defined as $|(K_{par} - K_{diag})|/K_{par}$, where K_{par} is one of the parameterization (I)–(IX); r^2 is based on linear regression using 200 points across all cases that is repeated 5000 times). Boxes and whiskers come in pairs, with the one on the left (right) corresponding to the southern (northern) slope. Linear regressions are done over the slope regions only (gray shading; similar to Fig. 1). In panels a and d, the estimates I–IX are scaled by constant a_1 optimized to match the mid-basin diffusivity, and in addition we use $a_T = 0.5$ (for VII–IX), and $a_2 = 2$ (for IX). The a_1 values are 0.1, 1.17, 0.09, 0.31, 3.77, 0.25, 0.66, 0.25, and 0.25 for estimates I–IX, respectively. In panels b and e, the dashed gray lines correspond to 25%, 50%, 100% absolute relative error.

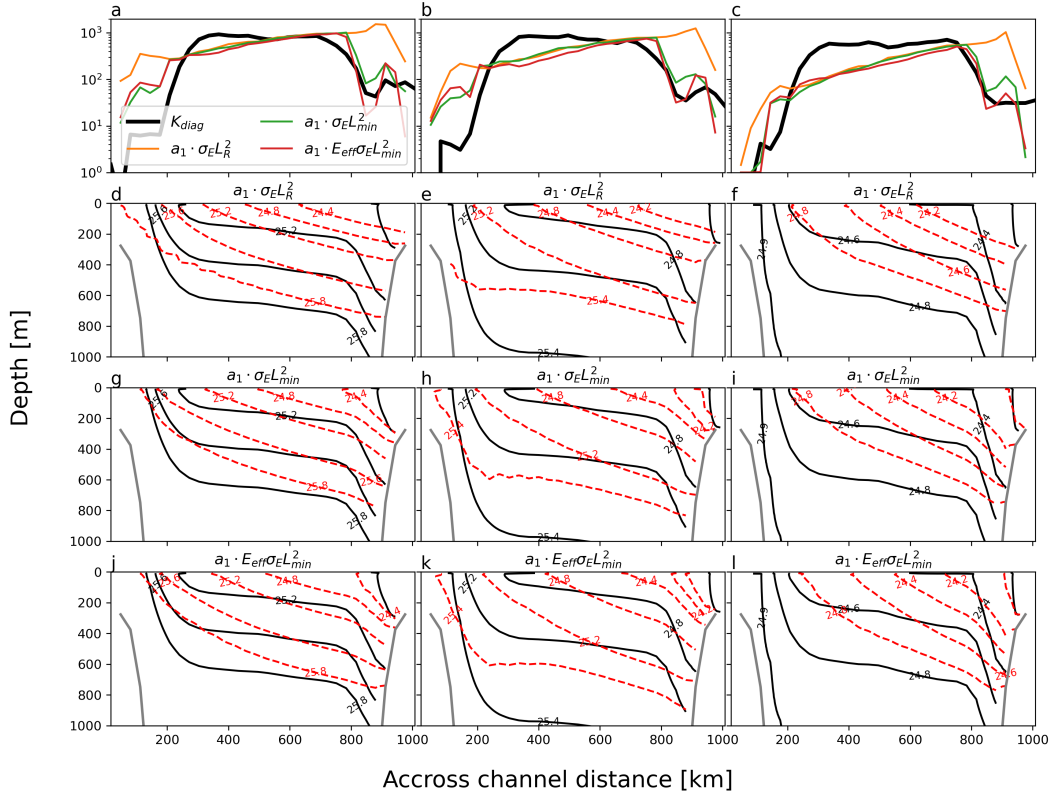


Figure 5. Buoyancy diffusivity (top row) and potential density anomaly (referenced to 0 dbar) in the upper 1000 m of the coarse-resolution channel simulation compared to the high-resolution simulation (black line; coarse-grained to the coarse resolution grid). The different columns show experiments with different stratification such that the initial conditions are the same as for Exp 3, 6 and 9 in the left, middle and right columns, respectively (the initial stratification decreases to the right). For panels d-l, title indicates the parameterization. Bottom topography is indicated with a gray line

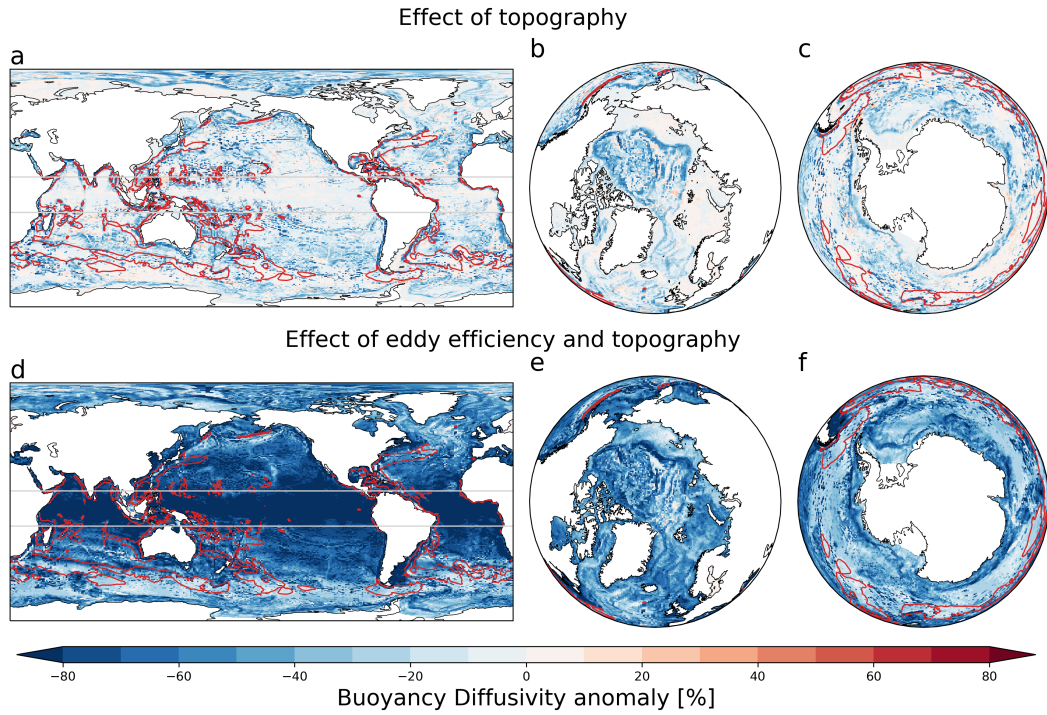


Figure 6. Anomalies from the control case in parameterized (depth-averaged) GM diffusivity due to implementation of (top row) the topographic Rhines scale and (bottom row) eddy efficiency in addition to the topographic Rhines scale. Red contours show the $1000 \text{ m}^2 \text{ s}^{-1}$ isoline for diffusivity in the control case and light gray contours show areas in the tropics where the grid size is smaller than the internal deformation radius and therefore the resolution function (Hallberg, 2013) reducing the GM coefficient is in effect.

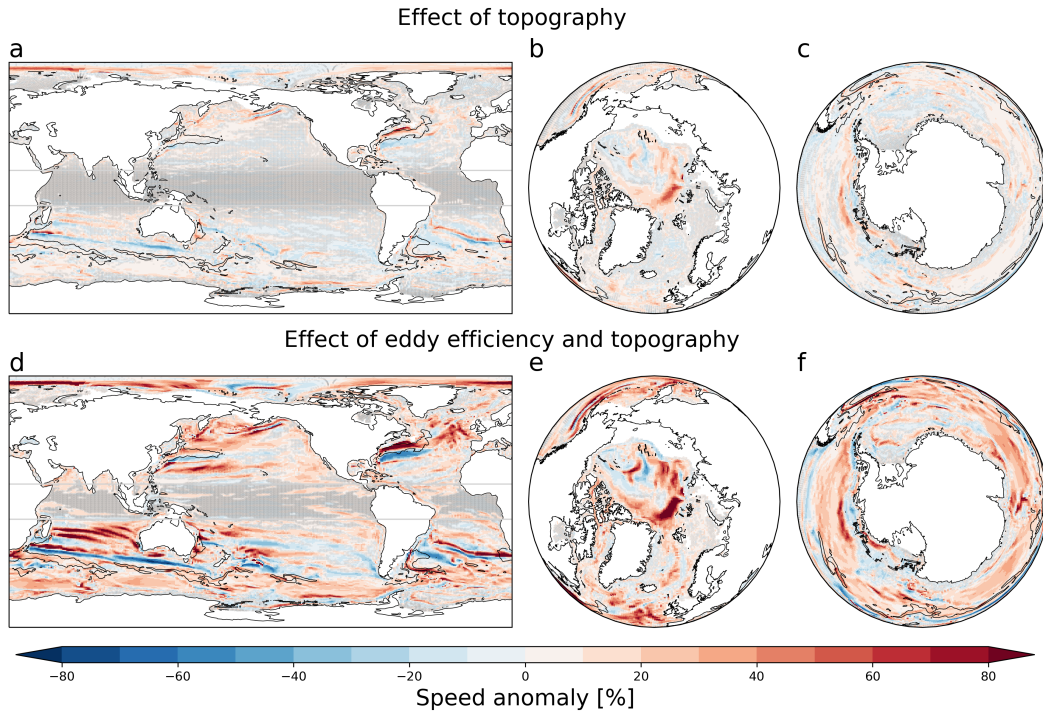


Figure 7. Flow speed anomalies from the control case at 100–200 m depth due to implementation of: (top row) the topographic Rhines scale and (bottom row) eddy efficiency in addition to the topographic Rhines scale. Black contours show the 0.25 m s^{-1} isolines for observational estimate of the quasi-geostrophic current speed (Buongiorno Nardelli, 2020) in the same 100–200 m depth interval. Gray dots mark grid cells where 30 year mean is not significantly different from the control case at 5% significance level (student’s t-test).

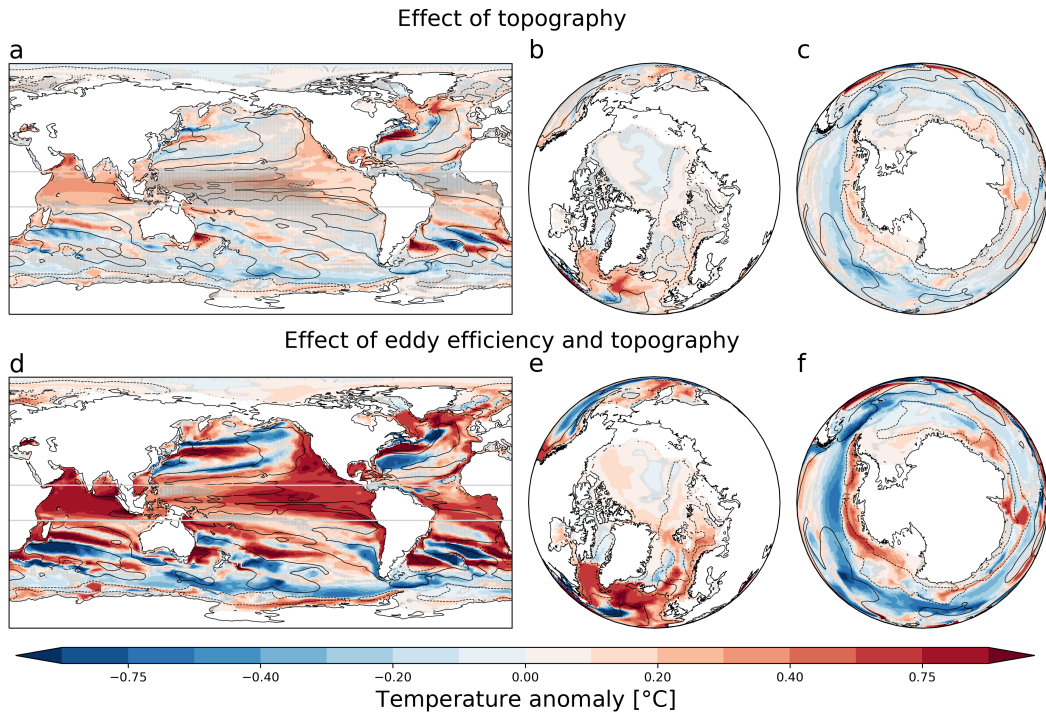


Figure 8. Temperature anomalies from the control case between 100–200 m depth due to implementation of: (top row) the topographic Rhines scale and (bottom row) eddy efficiency in addition to the topographic Rhines scale. Black contours show the $\pm 1^{\circ}\text{C}$ (solid/dashed) isoline for the control case bias relative to the WOA observations. Therefore, whenever solid (dashed) contours surround blue (red) areas the bias is reduced. Gray dots mark grid cells where 30 year mean is not significantly different from the control case at 5% significance level (student’s t-test).

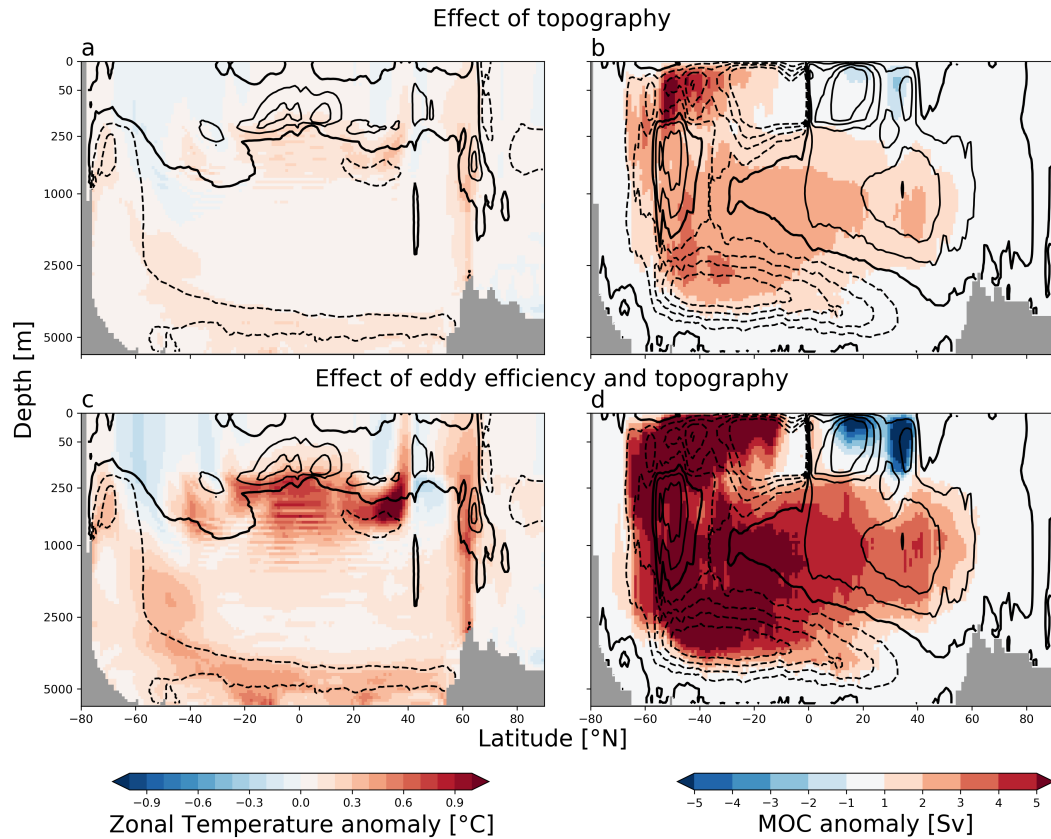


Figure 9. Zonal-mean temperature anomalies (left panels) and global meridional overturning stream function (MOC) anomalies (right panels), relative to the control simulation, due to implementation of: (top row) the topographic Rhines scale and (bottom row) eddy efficiency in addition to the topographic Rhines scale. For temperature, black contours show the control case bias relative to the WOA observations in 0.25°C intervals (dashed for negative, solid for positive, the thick solid curve shows the zero contour). Therefore, whenever solid (dashed) contours surround blue (red) areas the bias to the observations is reduced. For the MOC, the contours show the control case MOC at 5 Sv intervals with the thick solid curve indicating the 0 Sv contour. Therefore solid (dashed) contours surrounding red (blue) indicates intensifying overturning. Similar to Figs. 7-8, a student's t-test is applied here, but gray dots are now shown as all values are significant at 5% level.

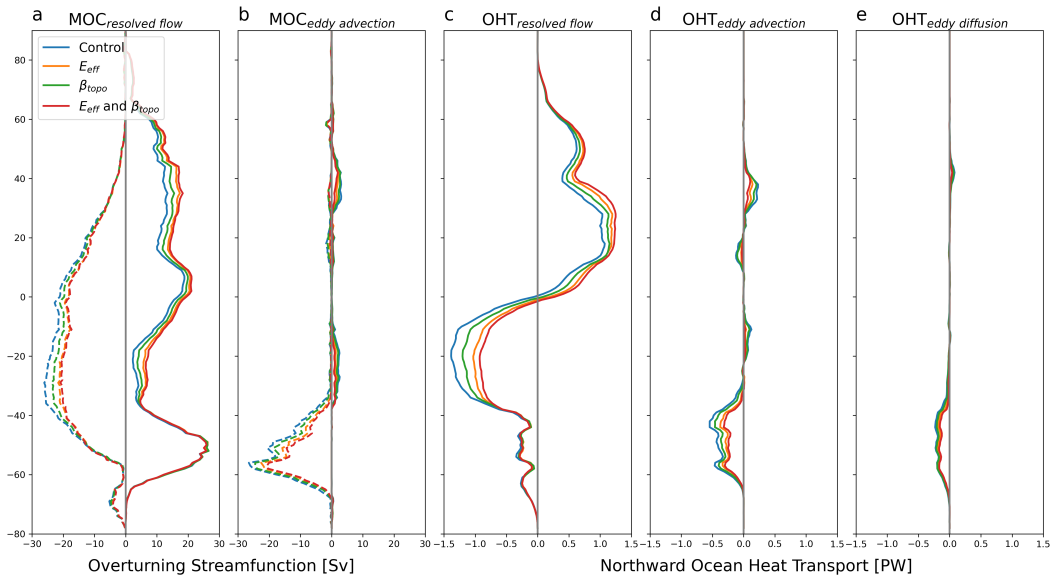


Figure 10. Resolved and eddy contributions to the global meridional overturning circulation (MOC, panels a and b) and to the global northward ocean heat transport (OHT, panels c–e). For the MOC we show the maximum (solid) and minimum (dashed) below 500 m to avoid the shallow surface overturning cells. For the OHT we show both advective and diffusive eddy contributions (panels d and e, respectively).